https://doi.org/10.5194/egusphere-2026-664
Preprint. Discussion started: 5 February 2026

Suppression of Orbital-Induced Polar Amplification by Lower GHG Concentrations Improves Mid-Holocene Simulations in PMIP4

Wenyuan Wang[1], Hanjie Fan[1,2], Xiaoming Hu[1,2], Kaiqiang Deng[1,2], and Song Yang[1,2]

[1]School of Atmospheric Sciences, Sun Yat-sen University, Southern Marine Science and Engineering Guangdong Laboratory (Zhuhai), Zhuhai 519082, China
[2]Guangdong Province Key Laboratory for Climate Change and Natural Disaster Studies, Sun Yat-sen University, Zhuhai 519082, China

Correspondence: Hanjie Fan (fanhj8@mail.sysu.edu.cn)

Abstract. The mid-Holocene (MH) provides a crucial window for investigating the impact of orbital forcing on climate. However, there is no consensus on MH temperature changes relative to the preindustrial. Substantial differences exist between the simulation results of the third and fourth phases of the Paleoclimate Model Intercomparison Project (PMIP3 and PMIP4), thereby increasing the uncertainty in MH temperature changes. To investigate these inter-generational discrepancies, we apply a climate feedback-response analysis method (CFRAM) to quantify the contributions of external forcings and internal feedbacks to MH temperature variations. Results suggest that the discrepancy is primarily driven by external forcings, but is substantially modulated by greenhouse gas (GHG)-conditioned nonlinear feedbacks. In PMIP3, orbital-forcing-induced warming more readily triggers strong polar amplification. In PMIP4, however, lower GHG concentrations lead to a colder background state and nonlinearly weaken key positive feedbacks, including sea-ice albedo and surface heat storage processes, thereby suppressing polar warming. This GHG-modulated feedback suppression brings PMIP4 simulations into closer agreement with multiple proxy reconstructions, supporting a relatively cooler MH. Our findings highlight the combined influence of orbital parameters and GHG forcing on MH temperature change and emphasize the nonlinear role of GHG changes in damping polar amplification. These results offer a process-based perspective for understanding the intergenerational differences among climate models.

1 Introduction

The mid-Holocene (MH, ~6 ka) represents a crucial stage of the current interglacial period. The Significant changes in Earth's orbital parameters during this period enhanced seasonal insolation differences (Berger, 1978; Wanner et al., 2015), resulting in a climate state that differed markedly from the pre-industrial period (PI) (Kaufman et al., 2020; Kaufman and Broadman, 2023; Steig, 1999). Therefore, the MH offers an ideal temporal window for investigating the impacts of orbital forcing on the Earth's climate (Chen et al., 2023a; Sun et al., 2023) and constitutes a key focus in paleoclimate research (Harrison et al., 2014; Burls and Sagoo, 2022). Numerous studies based on proxy-record reconstructions (Kaufman et al., 2020; Lin et al., 2019; Liu et al., 2025) and paleoclimate model simulations (Braconnot et al., 2007; Brierley et al., 2020; Otto-Bliesner et al., 2017; Lin et al., 2019; Shi et al., 2022) have been conducted to reveal the climatic characteristics of the MH.

https://doi.org/10.5194/egusphere-2026-664
Preprint. Discussion started: 5 February 2026

However, the temperature differences between MH and PI (MH minus PI, hereafter MH temperature changes) remain controversial (Chen et al., 2023a; Liu et al., 2014). Most traditional proxy records suggest that the MH was a warm period, with the annual mean temperature higher than the PI (Bartlein et al., 2011; Zhang et al., 2021; Chen et al., 2023b). In contrast, climate model simulations tend to indicate a general long-term warming trend since the early Holocene, with the MH being cooler than the PI (Jiang et al., 2012; Liu et al., 2014; Otto-Bliesner et al., 2017). This apparent discrepancy, known as the "Holocene temperature conundrum", poses a major challenge for understanding MH climate variability.

The Paleoclimate Modelling Intercomparison Project (PMIP) is an international collaborative initiative for numerical climate modeling that aimed at systematically examining climate model responses to paleoclimate boundary conditions and external forcing factors (Hargreaves et al., 2013; Jiang et al., 2015; Kageyama et al., 2018). Because the MH climate variability is a primary focus of the PMIP, the MH simulations are designated as a Tier-1 experiment (Braconnot et al., 2007; Harrison et al., 2015; Otto-Bliesner et al., 2017). The third phase of PMIP (PMIP3), in collaboration with the fifth phase of the Coupled Model Intercomparison Project (CMIP5) (Emori et al., 2016), focused on the impacts of orbital parameter changes during the MH on the global climate system, with a particular emphasis on the monsoon system and high-latitude temperature variations (Harrison et al., 2015; Taylor et al., 2012). The fourth phase of PMIP (PMIP4) further strengthened its integration with the sixth phase of CMIP (CMIP6) (Harrison et al., 2015; Kageyama et al., 2018; Otto-Bliesner et al., 2017). Building on PMIP3, the MH experiments in PMIP4 expanded their objectives to better simulate observed forcings and evaluate the models' predictive skill for past climate changes (Brierley et al., 2020; Harrison et al., 2015; Kageyama et al., 2018; Otto-Bliesner et al., 2017). Compared with PMIP3-CMIP5, PMIP4-CMIP6 employed climate models with higher resolutions and greater complexity (Zelinka et al., 2020), as well as more precise reconstructions of orbital parameters and greenhouse gas (GHG) concentrations (Bruno and Joos, 1997; Eyring et al., 2016; Otto-Bliesner et al., 2017) (Table 1).

Notably, PMIP3 and PMIP4 exhibit significant discrepancies in their simulations of MH temperature changes. Compared with the pronounced warming change in mid-to-high latitudes simulated by most PMIP3 models, the majority of PMIP4 models show widespread cooling during the MH, with a global mean temperature difference of about 0.28 K between the two generations (Brierley et al., 2020; Otto-Bliesner et al., 2017) (Figs. A1a-c). In the Northern Hemisphere midlatitudes, where the "Holocene temperature conundrum" is most contentious (Kaufman and Broadman, 2023; Bova et al., 2021; Chen et al., 2024), PMIP3 and PMIP4 display opposite features, with the former indicating warming and the latter cooling.

Previous studies have attempted to quantify the contributions from GHG decrease to the cooling in PMIP4 based on climate sensitivity and pattern scaling estimated by $2xCO_2$ warming experiments (Figs. A1a-c) (Dufresne et al., 2013; Brierley et al., 2020). However, this approach fails to fully explain the pronounced spatial discrepancies between PMIP3 and PMIP4, especially in the high latitudes of the Northern Hemisphere (Fig. A1f). This limitation likely stems from the non-linear nature of climate sensitivity (Friedrich et al., 2016), which predisposes such direct extrapolations from idealized warming experiments to the MH to systematic bias. Furthermore, the altered insolation conditions during the MH, resulting from changes in orbital forcing, concurrently influence the energy feedbacks and equilibrium state of the climate system (Kang and Yang, 2023). Therefore, a more precise and quantitative diagnostic approach is required to understand the temperature differences arising from GHG concentration differences between the two model generations.

https://doi.org/10.5194/egusphere-2026-664
Preprint. Discussion started: 5 February 2026

Table 1. Parameter settings in PMIP3-CMIP5 and PMIP4-CMIP6.

Parameter setting	PMIP3-CMIP5		PMIP4-CMIP6	
	MH	PI	MH	PI
Orbit	ecc=0.018682 obl=24.105° peri-180=0.87°	ecc=0.016724 obl=23.446° peri-180=102.04°	ecc=0.018682 obl=24.105° peri-180=0.87°	ecc=0.016724 obl=23.459° peri-180=100.33°
Solar(W/m2)	1365	1365	1361	1361
CO_2(ppm)	280	284.7	264.4	284.7
CH_4(ppb)	650	791.6	597.0	791.6
N_2O(ppb)	270	275.68	262.0	275.68
Ozone	Same as in PI	DECK PI	Same as in PI	DECK PI
Aerosols	Same as in PI	DECK PI	Same as in PI	DECK PI
Vegetation	Prescribed or interactive as in PI	DECK PI	Potential Vegetation, No urban, no crops	1850 CE Preindustrial Vegetation and crops
Topography	Modern	Modern	Modern	Modern
Ice Sheets	Modern	Modern	Modern	Modern

Moreover, while most previous researches have predominantly focused on annual mean temperature, the seasonal temperature evolution has received much less attention, despite its crucial role in shaping climate changes (Liu et al., 2025; Zhang et al., 2022). The discrepancies in MH temperature changes between PMIP3 and PMIP4 are particularly pronounced in boreal winter (Brierley et al., 2020), amplifying the uncertainties surrounding the "Holocene temperature conundrum" and hindering robust reconstruction of MH climate.

To address these gaps, we employ the climate feedback-response analysis method (CFRAM; Cai and Lu, 2009), a useful framework for diagnosing temperature changes and inter-model differences (Fan et al., 2021; Hu et al., 2017, 2020; Zhang et al., 2023). The CFRAM quantitatively decomposes temperature changes into contributions from individual radiative and non-radiative processes, placing them on a comparable basis. Based on the analysis using this approach, we demonstrate that an accurate representation of GHG is essential to avoid overestimating the polar amplification effect caused by insolation changes during the MH.

This study is structured as follows. Section 2 presents the data and methods applied. Section 3 compares the annual mean MH temperature changes between PMIP3 and PMIP4 and apply the CFRAM to quantify the contributions of different feedback mechanisms to their differences, interpreting the underlying physical causes. Section 4 extends this approach to seasonal temperature changes to elucidate their distinct driving mechanisms. Section 5 comprehensively evaluates the performance of both model generations by comparing their simulations with proxy records to assess their reliability. Conclusions are given in section 6.

https://doi.org/10.5194/egusphere-2026-664
Preprint. Discussion started: 5 February 2026

2 Data and Method

2.1 Climate models

The MH and PI simulation data from PMIP3-CMIP5 and PMIP4-CMIP6 are used in this study. The variables required for feedback process analysis include surface and air temperature, specific humidity, cloud fraction, liquid/ice water content in clouds, sensible and latent heat fluxes, upward and downward longwave fluxes at the surface, upward and downward shortwave fluxes at the surface, and upward longwave fluxes at the top of the atmosphere. In total, five PMIP3-CMIP5 models and seven PMIP4-CMIP6 models provide complete outputs of these variables, which are available for our analysis (Table 2). All climate data were obtained from the official CMIP6 and CMIP5 archives (https://esgf-node.llnl.gov/). The data for each model retains its original spatial resolution during CFRAM calculations. To ensure comparability across models, the surface temperature and CFRAM outputs from all models were interpolated onto a common 144×92 grid using bilinear interpolation.

In this study, the difference in surface temperature between the MH and PI (MH minus PI) is defined as the simulated MH temperature change. The MH and PI climatologies are defined as the averages over the last 100 years of each model's MH and PI experiments, respectively.

2.2 Proxy data

We employ two types of MH temperature reconstructions, statistical reconstructions based on proxy records and machine learning-based reconstructions, to evaluate model-data consistency for PMIP3 and PMIP4.

The statistical reconstructions from proxy records (hereafter "proxy records") are derived from two datasets, both based on statistical approaches that quantitatively reconstruct past temperatures by developing transfer functions between modern indicators and temperature or by applying modern analogue methods. The first is the most recent Temperature 12k database (Kaufman et al., 2020), which contains 1,319 temperature time-series reconstructions encompassing a wide range of ecological, geochemical, and biophysical indicators. From this dataset, we extracted 157 annual, 54 summer (JJA), and 1 winter (DJF) anomalies of the MH (6.0 ± 0.5 ka) relative to the most recent millennium (0.5 ± 0.5 ka) for site-level comparison with PMIP3 and PMIP4 simulations (Figs. A2a–c). The second is a pollen-based MH temperature reconstruction dataset (Zhang et al., 2022), comprising 1,310 sites (542 in Europe, 191 in Asia, and 577 in North America), accompanied by a modern pollen dataset of 13,077 surface samples compiled from North America, Europe, East Asia, and the Eurasian pollen databases. The reconstructions provide annual mean, boreal summer (JJA) and winter (DJF) temperatures for both the MH and the modern periods. From these data, a total of 339 MH anomalies relative to the most recent millennium, including annual, summer, and winter values, were extracted for site-level comparison with both model generations.

Given that traditional proxy-based reconstructions may be influenced by seasonal signals (Chen et al., 2023a), our study additionally incorporates a machine learning-based reconstruction dataset (hereafter brGDGT-DLNN) (Liu et al., 2025) to provide a more comprehensive understanding of MH temperature changes. This dataset is based on brGDGT (branched glycerol dialkyl glycerol tetraether) records from 33 sediment profiles worldwide (including loess, lakes, and peat). Using a deep learning neural network (DLNN) approach that integrates multiple brGDGT indices and compound percentage data, this dataset

https://doi.org/10.5194/egusphere-2026-664
Preprint. Discussion started: 5 February 2026

Table 2. PMIP3-CMIP5 and PMIP4-CMIP6 model informations.

PMIP-CMIP	Model acronym	Reference	Institution	Spatial resolution
PMIP3-CMIP5 r1i1p1	**BCC-CSM1-1**	(Wu et al., 2014)	Beijing Climate Center, China Meteorological Administration	320×160
PMIP3-CMIP5 r1i1p1	**CCSM4**	(Sahany et al., 2019)	National Center for Atmospheric Research	288×192
PMIP3-CMIP5 r1i1p1	**FGOALS-s2**	(Li et al., 2013)	LASG, Institute of Atmospheric Physics, Chinese Academy of Sciences and CESS, Tsinghua University	128×108
PMIP3-CMIP5 r1i1p1	**GISS-E2-R**	(Ullman et al., 2014)	NASA Goddard Institute for Space Studies, USA	144×90
PMIP3-CMIP5 r1i1p1	**MRI-CGCM3**	(Yukimoto et al., 2012)	Meteorological Research Institute	320×160
PMIP4-CMIP6 r1i1p1f1	**AWI-ESM-1-1-LR**	(Shi et al., 2023)	Alfred Wegener Institute, Helmholtz Centre for Polar and Marine Research, Germany	192×96
PMIP4-CMIP6 r1i1p1f1	**FGOALS-f3-L**	(Zheng et al., 2020)	LASG, Institute of Atmospheric Physics, Chinese Academy of Sciences, China	288×180
PMIP4-CMIP6 r1i1p1f1	**GISS-E2-1-G**	(Kelley et al., 2020)	NASA Goddard Institute for Space Studies, USA	144×90
PMIP4-CMIP6 r1i1p1f2	**MIROC-ES2L**	(Ohgaito et al., 2021)	JAMSTEC, AORI, NIES, R-CCS, Japan	128×64
PMIP4-CMIP6 r1i1p1f1	**MPI-ESM1-2-LR**	(Mauritsen et al., 2019)	Max Planck Institute for Meteorology, Germany	144×96
PMIP4-CMIP6 r1i1p1f1	**MRI-ESM2-0**	(Yukimoto et al., 2019)	Meteorological Research Institute, Japan	320×160
PMIP4-CMIP6 r1i1p1f1	**NorESM2-LM**	(Seland et al., 2020)	Norwegian Climate Centre, Norway	144×96

https://doi.org/10.5194/egusphere-2026-664
Preprint. Discussion started: 5 February 2026

provides independent reconstructions of Holocene annual mean and boreal summer temperatures across the Northern Hemisphere midlatitudes (20°N-50°N) (Figs. A2a–b).

Model-data consistency is evaluated for MH temperature changes in the annual mean, boreal summer, and winter. Due to the limited spatial coverage and representativeness of proxy records in certain regions, the analysis is restricted to the Northern Hemisphere of 10°-80°N, where proxy records are more abundant. The brGDGT-DLNN dataset is further evaluated only within the 20°-50°N latitudinal band.

2.3 CFRAM

We applied the CFRAM (Cai and Lu, 2009) to quantify the contributions of different climate processes to MH surface temperature changes and to investigate the physical mechanisms underlying the intergenerational model differences. The CFRAM is based on an atmosphere-surface column system, assuming that the system is in energy balance. Within this framework, the total temperature change is linearly decomposed into partial temperature changes (PTCs) driven by different radiative and non-radiative processes. Under temperature changes, the variation in net radiative flux at equilibrium can be balanced by the sum of radiative flux changes independent of temperature and non-radiative energy flux changes, expressed as follows:

$$\Delta\left(\frac{\partial E}{\partial t}\right) = \Delta(S-R) + \Delta Q_{\text{non-rad}} \tag{1}$$

$\Delta\left(\frac{\partial E}{\partial t}\right)$ represents the difference in energy storage between the two states; the vertical radiative energy flux independent of temperature ($Q_{\text{rad}} = S - R$) can be derived from the difference between the vectors of vertical convergence of the net solar radiation fluxes (S) and vertical divergence of the net longwave radiation fluxes (R). By applying a linear approximation, $\Delta(S-R)$ can be further decomposed into partial differences attributable to various feedback processes:

$$\Delta(S-R) = \Delta^{\text{GHG}}(S-R) + \Delta^{\text{AL}}S + \Delta^{\text{WV}}(S-R) + \Delta^{\text{CLDS}}(S-R) + \Delta^{\text{CLDL}}(S-R) - \left(\frac{\partial R}{\partial T}\right)\Delta T \tag{2}$$

The superscripts GHG, AL, WV, CLDS, and CLDL denote radiative flux responses to changes in the following factors:greenhouse gas concentrations (CO_2, N_2O, CH_4), solar radiation, water vapor, cloud shortwave radiation, and cloud-top longwave radiation, respectively. Here, $\left(\frac{\partial R}{\partial T}\right)$ is the Planck feedback matrix, with its j-th column representing the vertical profile of LW radiative flux changes when the j-th layer is heated by 1 K. $\Delta Q_{\text{non-rad}}$ represents changes in non-radiative energy fluxes, which can be further decomposed into the following components:

$$\Delta Q_{\text{non-rad}} = \Delta Q^{\text{ATM}} + \Delta Q^{\text{SRF}} + \Delta Q^{\text{SH}} + \Delta Q^{\text{LH}} \tag{3}$$

Here, ΔQ^{ATM} corresponds to the vertical profile of energy convergence changes induced by atmospheric convection and large-scale circulation. ΔQ^{SRF} denotes the residual term required to close the surface energy budget in the CFRAM framework.

https://doi.org/10.5194/egusphere-2026-664
Preprint. Discussion started: 5 February 2026

This term primarily reflects the effects of surface heat storage and unresolved heat transport processes over both oceanic and terrestrial surfaces, including ocean heat storage, ocean heat transport, soil heat storage, and runoff. Owing to the dominant role of the ocean in the global energy balance, this term is largely governed by oceanic variations. ΔQ^{SH} and ΔQ^{LH} denote changes in energy convergence arising from variations in sensible and latent heat fluxes, respectively. Substituting Eqs. (2) and (3) into Eq. (1), rearranging the terms, and multiplying both sides by the inverse of the Planck feedback matrix $\left(\frac{\partial R}{\partial T}\right)$, we obtain:

$$\Delta T = \left(\frac{\partial R}{\partial T}\right)^{-1} \Big[\Delta^{\mathrm{GHG}}(S-R) + \Delta^{\mathrm{AL}} S + \Delta^{\mathrm{WV}}(S-R) + \Delta^{\mathrm{CLDS}}(S-R) + \Delta^{\mathrm{CLDL}}(S-R) + \Delta Q^{\mathrm{ATM}} + \Delta Q^{\mathrm{SRF}} + \Delta Q^{\mathrm{SH}} + \Delta Q^{\mathrm{LH}}\Big] \tag{4}$$

We employed the Fu–Liou radiative transfer model (Fu et al., 1997) to evaluate the radiative energy perturbation terms in Eq. (4): in one case, all input fields were taken from the mean state of the control climate, and in the other, from the mean state of the warmed climate. Subsequently, Eq. (4) was simplified to:

$$\Delta T = \Delta T^{\mathrm{GHG}} + \Delta T^{\mathrm{WV}} + \Delta T^{\mathrm{AL}} + \Delta T^{\mathrm{CLDS}} + \Delta T^{\mathrm{CLDL}} + \Delta T^{\mathrm{ATM}} + \Delta T^{\mathrm{SRF}} + \Delta T^{\mathrm{SH}} + \Delta T^{\mathrm{LH}} \tag{5}$$

Each term in Eq. (5) is defined as the product of $\left(\frac{\partial R}{\partial T}\right)$ multiplied the perturbation of net radiative flux convergence associated with each radiative term or by the change in energy flux convergence due to non-radiative terms, respectively. Equation (5) allows for grid-by-grid calculations.

By applying the CFRAM, the surface temperature changes during the MH can be decomposed into two parts: (1) PTCs directly caused by changes in external forcing, and (2) PTCs resulting from the individual effects of radiative and non-radiative processes. These changes were obtained by solving a linearized infrared radiative transfer model. In this study, the radiative feedback processes considered include surface albedo (AL), water vapor (WV), cloud feedback (CLD), greenhouse gases (GHG), and solar radiation (SR). The non-radiative processes include large-scale atmospheric circulation and convection (ATM), surface heat storage and transport processes (SRF), and surface heat fluxes effect (HF), with HF consisting of sensible (SH) and latent heat (LH) fluxes. In addition, to better characterize the overall temperature response to external forcing during the MH—particularly the combined influence of GHG and SR changes—we define a new index, external forcing (EF), as the sum of the GHG and SR feedbacks. Since the prescribed GHG values in some models differ from those specified by PMIP3 and PMIP4 protocols, we conducted the CFRAM analysis using the actual GHG parameters implemented in the simulations (Table A1).

https://doi.org/10.5194/egusphere-2026-664
Preprint. Discussion started: 5 February 2026

3 Annual temperature differences between PMIP3 and PMIP4

3.1 Annual mean MH temperature changes in PMIP3 and PMIP4

We first analyze the annual mean MH temperature changes in the two generations of models and compared their differences. The five PMIP3 simulations are generally consistent with the MME (Fig. A3a), showing pronounced warming during the MH in high-latitude regions, particularly the Arctic and parts of the Southern Ocean, while most tropical to subtropical regions exhibit slight cooling. The PMIP3 MME global annual mean MH temperature change is approximately +0.1 K (Fig. 1a). In contrast, the seven PMIP4 models and their MME simulate an overall cooling during the MH (Fig. A3b). Most land areas in the Northern Hemisphere exhibit cooling compared to the PI, except for slight warming in specific high-latitude regions, with a global annual mean temperature decrease of about 0.3 K (Fig. 1b). The model simulations analyzed in this study are broadly consistent with previous conclusions based on the full ensemble of models (Brierley et al., 2020).

The differences in MH temperature changes between PMIP3 and PMIP4 are pronounced and exhibit a latitudinal dependence, increasing markedly toward higher latitude (Fig. 1). In low-latitude regions (0°-30°), both model generations simulate cooling, with minimal differences between them. A pronounced intergenerational discrepancy emerges in the mid-latitude regions (30°-60°): PMIP3 shows warming in certain regions (Fig. 1a), whereas PMIP4 exhibits overall cooling, yielding a mean intergenerational difference of about 0.2 K (Fig. 1b). The contrast is most extreme in the high-latitude regions (60°-90°). PMIP3 simulates robust warming across both the Arctic and Antarctic, whereas warming in PMIP4 is substantially weaker and confined mainly to the Arctic Pole and the Amundsen Sea sector. Consequently, the intergenerational temperature difference in high latitudes exceeds 0.6 K (Fig. 1c), underscoring polar regions as the primary locus of the modeling discrepancy.

3.2 Feedback contributions to annual mean temperature changes

Using the CFRAM, we quantify the contributions of individual feedback processes to MH temperature changes across PMIP3 and PMIP4 models (Fig. 2). The external forcings, SR and GHG, establish the initial thermal perturbation. SR causes comparable global mean warming in both generations, but GHG induces a much stronger global cooling in PMIP4. This enhanced GHG cooling in PMIP4 subsequently modulates several feedback processes: AL, WV, and SRF act to amplify the intergenerational differences, while HF partially offsets the effects of above processes. In contrast, CLD and ATM play minor roles in the inter-generation contrast. We next examine the spatial patterns of these feedback processes.

The spatial patterns of individual feedback processes are broadly similar between PMIP3 and PMIP4 (Fig. 3). SR generates a characteristic pattern of polar warming and mid-to-low latitude cooling (Figs. 3c and 3l), whereas GHG exerts a nearly uniform cooling across latitudes (Figs. 3b and 3k). In response, both AL and WV amplify the temperature pattern induced by external forcings: AL enhances high-latitude warming, particularly over ice-covered regions (Figs. 3d and 3m), whereas WV intensifies mid-to-low latitude cooling (Figs. 3e and 3n). WV also contributes to an interhemispheric asymmetry, warming the Northern Hemisphere while cooling the Southern Hemisphere. Other processes, CLD, ATM, SRF and HF, exhibit less organized spatial structures. Yet, SRF and HF display more identifiable zonal mean features: SRF causes low-latitude cooling and mid-to-high-

https://doi.org/10.5194/egusphere-2026-664
Preprint. Discussion started: 5 February 2026

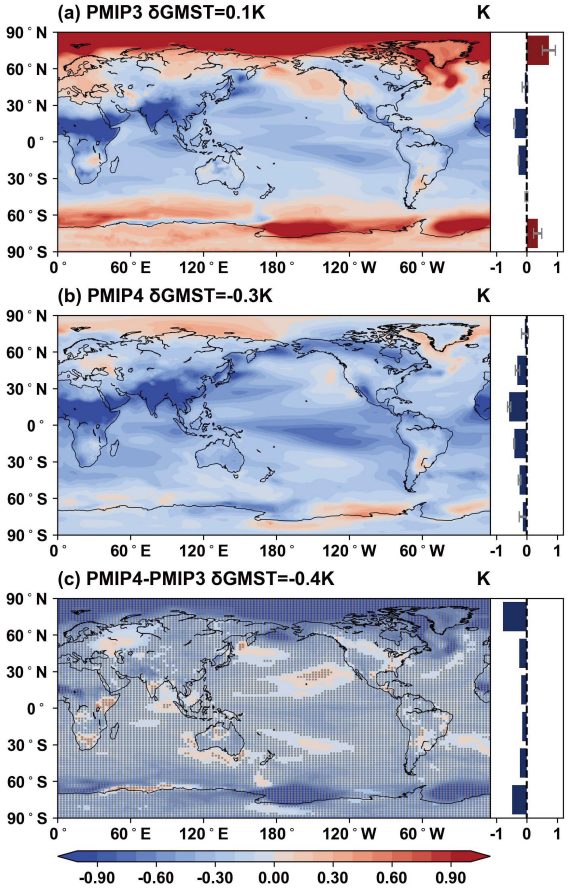

Figure 1. Temperature changes (MH-PI) and differences in the two generations of models. (a) and (b) show the MH temperature changes simulated by the PMIP3 MME and PMIP4 MME, respectively. (c) shows the difference between PMIP4 and PMIP3. Gray dots indicate the significant differences at the 95% confidence level (Student's t-test; $p < 0.05$).

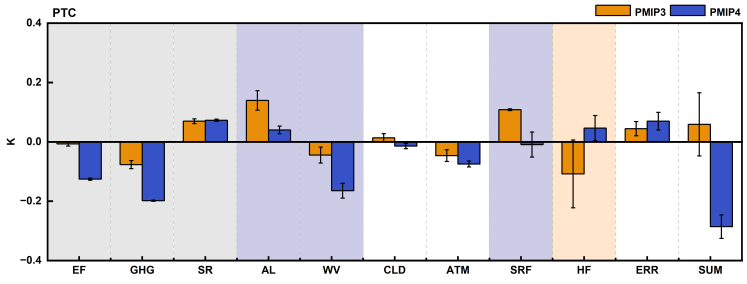

Figure 2. Contributions of individual feedback processes to annual mean temperature changes in the PMIP3 and PMIP4 MMEs.

https://doi.org/10.5194/egusphere-2026-664
Preprint. Discussion started: 5 February 2026

latitude warming (Figs. 3h and 3q), particularly in the Southern Hemisphere, while HF counteracts this pattern, demonstrating a compensatory role in the energy budget (Figs. 3i and 3r).

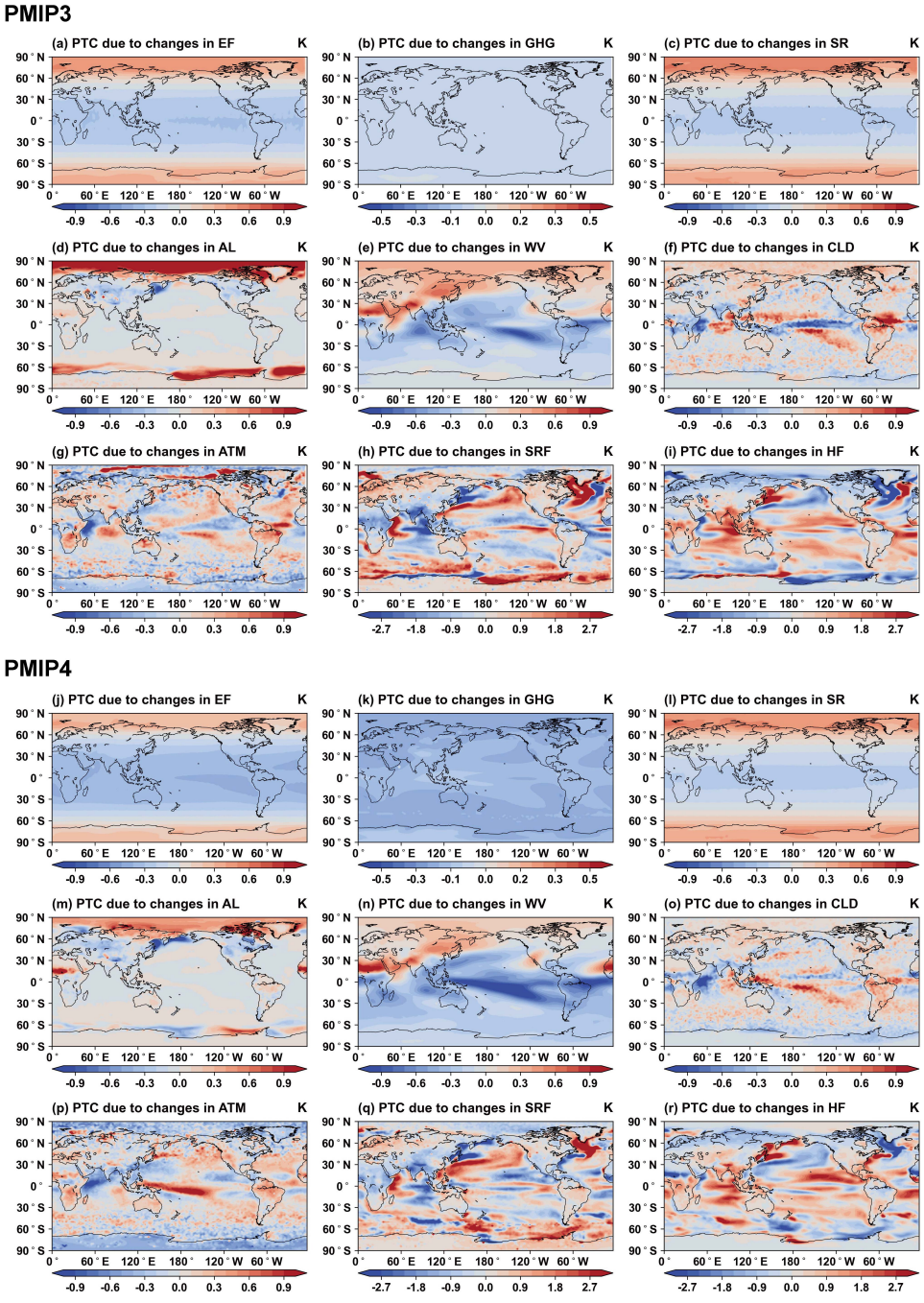

Figure 3. Contributions of individual feedback processes to temperature changes in the PMIP3 and PMIP4 MMEs.

https://doi.org/10.5194/egusphere-2026-664
Preprint. Discussion started: 5 February 2026

The key to understanding the latitudinal structure of the intergenerational difference lies not in the direct, uniform GHG cooling, but in how this cooling modulates the polar and tropical feedbacks (Fig. 4). In PMIP3, the net external forcing (SR + weak GHG) retains a pattern of distinct polar warming and low-latitude cooling (Fig. 4a). This pattern is then amplified by feedbacks: a strong AL response enhances high-latitude warming by ~0.6 K, while WV intensifies low-latitude cooling by ~0.3 K. In PMIP4, the stronger GHG cooling suppresses the initial polar warming. This leads to a much weaker cryospheric response and a reduced AL response (~0.3 K). But a stronger WV-induced cooling in mid-to-low latitudes (~0.5 K) (Fig. 4b). Concurrently, the cooler background state strengthens the WV-induced cooling in mid-to-low latitudes (~0.5 K). Crucially, the AL difference is highly concentrated in polar regions, thereby directly enhancing the latitudinal gradient of MH temperature changes (Fig. 4c). Beyond AL and WV, the non-uniform differences in SRF and HF also play a secondary, reinforcing role: the SRF difference pattern (cooler poles, warmer tropics) further enhances the latitudinal gradient, while the HF difference partially offsets it.

3.3 Mechanisms underlying annual mean temperature differences

We next elucidate the physical mechanisms of the WV, AL, and SRF feedback processes in contributing to the intergenerational differences. The WV feedback, a key positive feedback, amplifies the initial temperature changes by external forcings. The spatial patterns of WV-derived partial temperature change and the change in MH water vapor content are almost identical, implying their linear relationship (Fig. 5). PMIP3 simulations show a hemispheric asymmetry, with increased water vapor in the Northern Hemisphere and decreased vapor in the Southern Hemisphere, reinforcing a "warm north-cold south" temperature pattern (Fig. 5a). In PMIP4, the prescribed lower GHG concentrations cause a cooler mean climate state, which reduces the moisture-holding capacity in the atmosphere. This leads to a more substantial reduction in water vapor, particularly in the tropics and Southern Hemisphere, thereby strengthening the global cooling efficacy of the WV feedback (Figs. 5b and 5c).

The AL feedback is the primary driver of the divergent high-latitude temperature changes during the MH. While both generations experience polar-amplified warming due to changes in the SR, the resulting cryospheric changes differ markedly. In PMIP3, this warming triggers substantial reductions in sea ice concentration (SIC) in both hemispheres (Fig. 6d) and a slight decline in Northern Hemisphere snow cover (SNC) (Fig. 6g). The extensive retreat of ice and snow efficiently lowers the surface albedo, initiating a strong positive feedback that amplifies local warming (Fig. 6a). In PMIP4, however, the cooler background climate resulting from lower GHG concentrations buffers the cryosphere against the orbital forcing. Consequently, SIC and SNC remain relatively higher than in PMIP3 (Figs. 6e, 6h). This muted cryospheric retreat leads to a much weaker albedo reduction (Fig. 6b), directly suppressing the polar amplification mechanism and explaining the substantially lower annual mean high-latitude temperatures in PMIP4 relative to PMIP3.

The SRF feedback, particularly through its impact on ocean heat convergence, contributes significantly to the intergenerational difference, especially around Antarctica. The mechanism originates from the increased obliquity during the MH (Berger, 1978), which reduces the meridional insolation gradient and weakens the Southern Hemisphere westerly winds. In PMIP3, pronounced easterly wind anomalies emerge south of 60°S (Fig. 7a). Coupled with freshwater input from enhanced ice-sheet melt (Fig. 7d), these anomalies act to weaken the Antarctic Circumpolar Current (ACC) (Lamy et al., 2019; Park et al., 2018)

https://doi.org/10.5194/egusphere-2026-664
Preprint. Discussion started: 5 February 2026

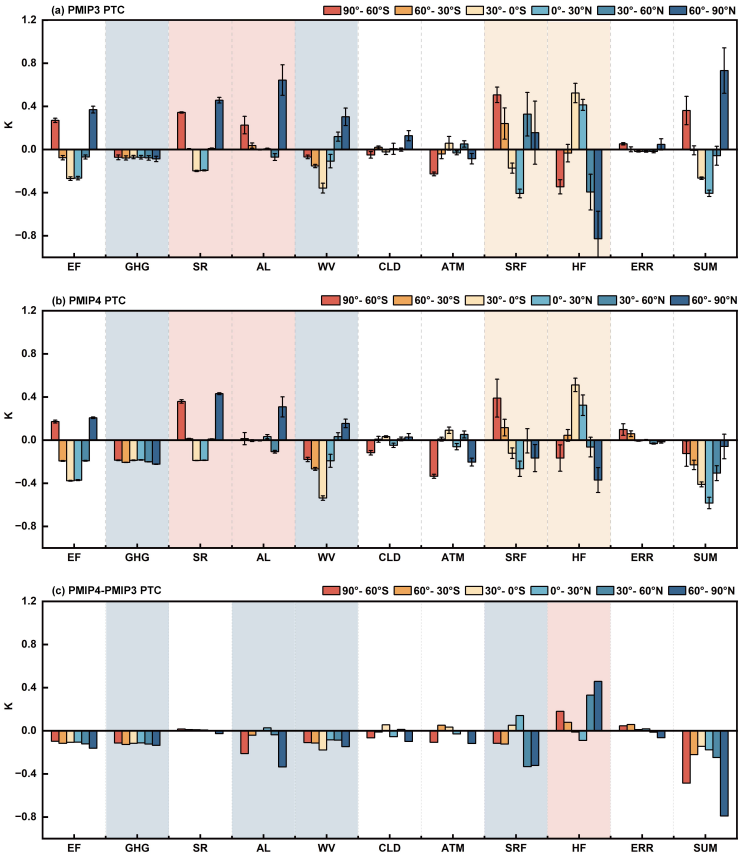

Figure 4. Latitudinal contributions of individual feedback processes to annual-mean temperature changes (MH-PI) in the PMIP3 and PMIP4 MMEs. Bars represent the mean temperature contribution of each feedback term, averaged within six latitude bands (90°S-60°S, 60°S-30°S, 30°S-0°, 0°-30°N, 30°-60°N, 60°-90°N). Panels show (a) PMIP3, (b) PMIP4, and (c) PMIP4 minus PMIP3. Error bars denote inter-model spread (±1 standard deviation).

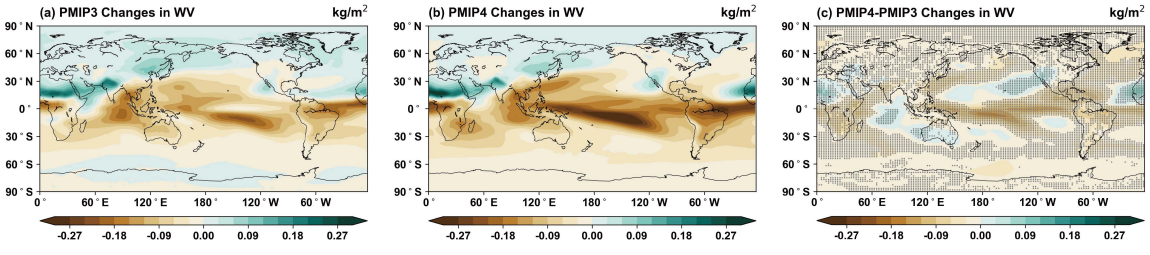

Figure 5. Column-integrated atmospheric water vapor changes (MH-PI). (a) and (b) show water vapor changes in PMIP3 and PMIP4, respectively; (c) shows the difference between PMIP4 and PMIP3. Gray dots indicate the significant differences at the 95% confidence level (Student's t-test; $p < 0.05$).

https://doi.org/10.5194/egusphere-2026-664
Preprint. Discussion started: 5 February 2026

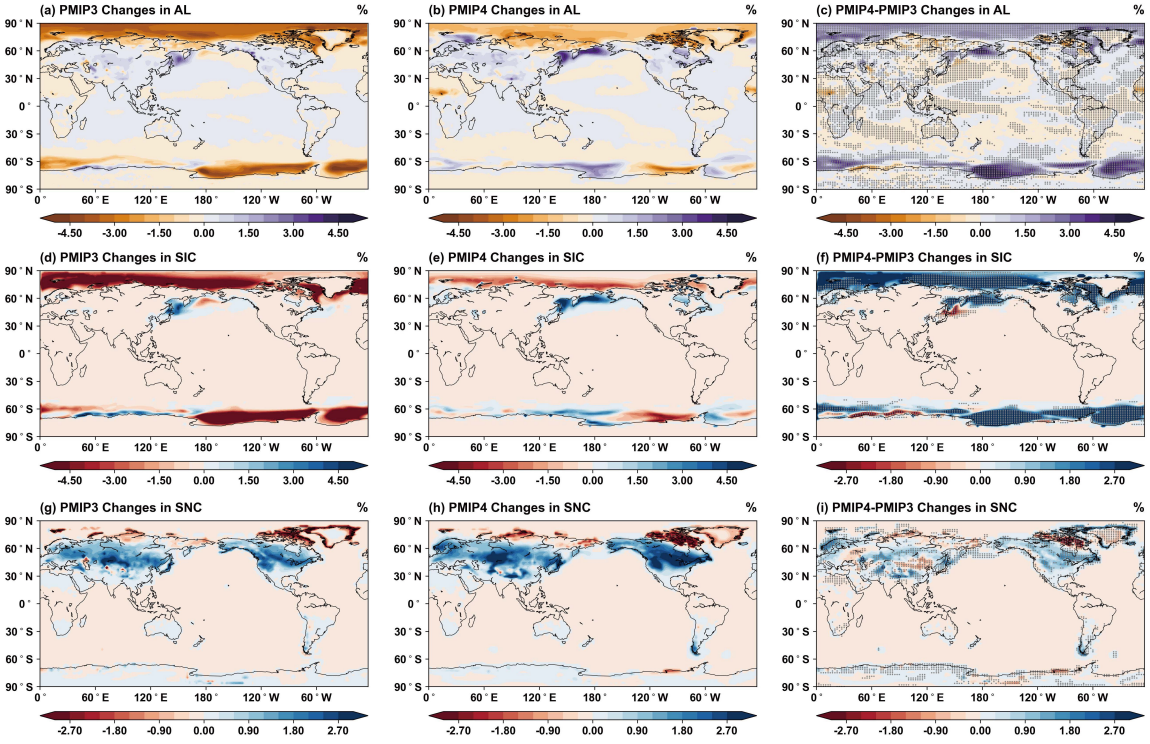

Figure 6. AL, SIC, and SNC changes (MH-PI). (a)-(c) AL changes in PMIP3, PMIP4, and PMIP4-PMIP3, respectively. (d)-(f) and (g)-(i) present the corresponding changes in SIC and SNC. Gray dots indicate the significant differences at the 95% confidence level (Student's *t*-test; $p < 0.05$).

and drives a southward shift of the Antarctic Polar Front (Fig. 7g). This ocean dynamical adjustment enhances heat transport towards the high-latitude Southern Ocean, manifesting as a warming contribution from SRF (Fig. 7a). In PMIP4, the same obliquity forcing operates, but the weaker background polar amplification alters the response of climate system. The wind stress weakening is considerably less pronounced (Fig. 7c), and consequently, the ACC strength and the position of the Polar Front remain largely unchanged (Fig. 7h), leading to a cooler thermal state in the ocean (Fig. 7e). This demonstrates that the sensitivity of the Southern Ocean to obliquity forcing (Yin and Berger, 2012) is state-dependent: the efficacy of this orbitally forced ocean warming mechanism is greatly diminished under the cooler PMIP4 background climate and weaker polar amplification, leading to a weaker SRF feedback and less Antarctic warming.

Notably, the CFRAM analysis reveals that the SRF feedback also plays a key role in explaining the Arctic temperature differences between the two generations of models (Fig. 4c). However, the annual-mean analysis presented here does not reveal a large-scale, coherent pattern of ocean heat transport change in the Northern Hemisphere comparable to that in the Southern Ocean. This indicates that dynamical ocean contributions in the Arctic may be weaker on an annual mean basis or may be dominated by processes that are highly seasonal in nature. The potential role of seasonally modulated ocean heat

https://doi.org/10.5194/egusphere-2026-664
Preprint. Discussion started: 5 February 2026

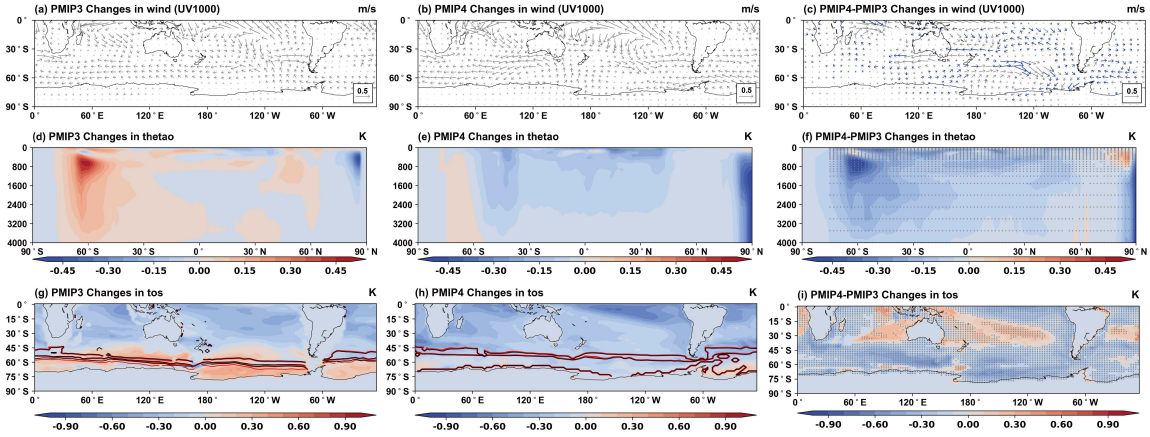

Figure 7. Changes in 1000hPa wind, potential temperature of sea water (thetao), and sea surface temperature (tos) (MH-PI). (a)-(c) 1000hPa wind changes in PMIP3, PMIP4, and PMIP4-PMIP3, respectively; (d)-(f) and (g)-(i) present the corresponding changes in thetao and tos; In (g) and (h), the red lines indicate Southern Ocean fronts identified from the temperature field during the MH, from north to south: nSAF (northern Subantarctic Front), sSAF (southern Subantarctic Front), and PF (Polar Front) (Giglio and Johnson, 2016); black lines indicate the PI fronts. Gray dots indicate the significant differences at the 95% confidence level (Student's t-test; $p < 0.05$), for the scalar fields (thetao and tos) and 1000 hPa wind vectors, respectively.

transport and its interaction with sea ice dynamics in driving Arctic temperature evolution during the MH will be explored in the following section on seasonal changes.

4 Seasonal temperature differences between PMIP3 and PMIP4

4.1 Seasonal temperature changes in PMIP3 and PMIP4

We examine the seasonal MH temperature changes simulated in PMIP3 and PMIP4. During the MH, precessional changes strongly enhance the seasonal contrast in insolation (Berger, 1978). Since the cooling from reduced GHG concentrations is persistent across seasonal evolution, the SR component dominates and generates a strongly seasonally dependent EF. Intuitively, this should produce a direct "summer warming-winter cooling" response, especially in high latitudes where the forcing amplitude is greatest (Fig. A4). Consistent with this, previous studies have noted the potential for substantial summer warming (Liu et al., 2025) and winter cooling (Dufresne et al., 2013; Brierley et al., 2020) in the Arctic during the MH. However, both model generations deviate from this expectation and show concurrent Arctic warming in both summer (JJA) and winter (DJF) (Fig. 8). PMIP3 presents pronounced JJA warming and notable DJF warming (Figs. 8a, 8d), whereas PMIP4 shows a more moderate, yet still warming, seasonal response (Figs. 8b, 8e). This paradoxical "year-round warming" signal, against a forcing pattern that favors seasonal contrast, points to the operation of strong intrinsic climate feedbacks that redistribute energy across seasons.

https://doi.org/10.5194/egusphere-2026-664
Preprint. Discussion started: 5 February 2026

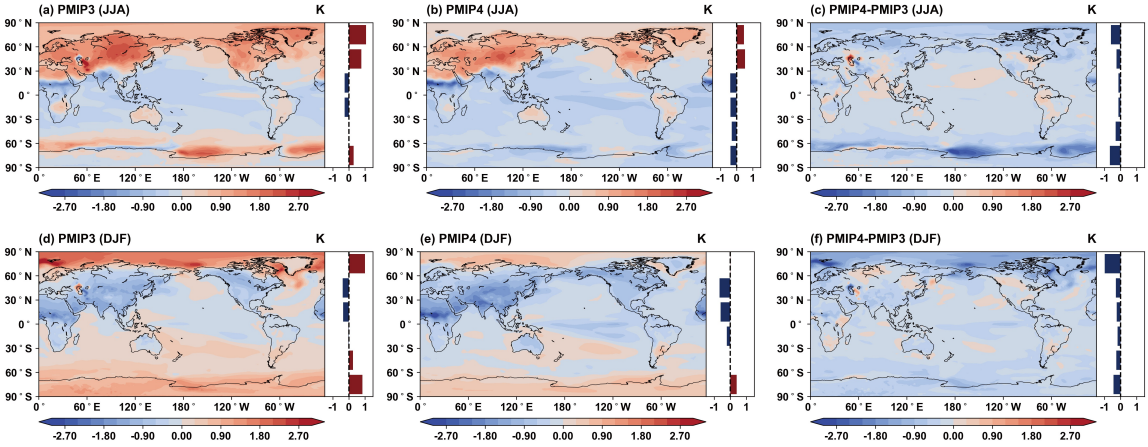

Figure 8. Seasonal temperature changes (MH-PI).

The unique Arctic response is further clarified by comparing zonal-mean EF with the actual temperature change (Fig. 9). At most latitudes, the temperature changes closely follow the seasonal cycle of the EF. North of 60°N, however, the seasonal temperature contrast weakens rather than intensifies. During boreal summer (JJA), although the EF peaks in the Arctic, the zonal-mean warming trend actually decreases with latitude (Fig. 9a). Conversely, in winter (DJF), when the EF turns negative, the Arctic exhibits pronounced warming that contradicts the direct radiative forcing (Fig. 9b). This pattern of constrained summer warming and enhanced winter warming is more evident in PMIP3, while the cooler PMIP4 simulations show a weaker and smoother seasonal response (Fig. 9c). The clear decoupling between the seasonal forcing and the local temperature response confirms that regional, non-radiative processes fundamentally reshape the Arctic energy budget across seasons.

4.2 Feedback contributions to seasonal temperature changes

To diagnose the processes behind this seasonal pattern, we use CFRAM to quantify the contributions of individual feedback processes. In JJA, Arctic warming is initiated directly by SR (Figs. 10a, 10e), and markedly amplified by the AL feedback (Figs. 10b, 10f). Critically, the SRF feedback, dominated by ocean heat content (OCH) changes, acts as a substantial heat sink in summer, partially offsetting the warming signal (Figs. 10c, 10g). This explains the constrained Arctic summer warming despite the substantial increase in SR. In DJF, the situation reverses. While SR and GHG forcings weaken markedly, the SRF/OCH feedback becomes the dominant heat source, releasing stored oceanic heat and counteracting the radiative cooling expected from external forcing, allowing the Arctic to remain warmer during the MH winter than the PI winter.

This seasonal reversal is the hallmark of the Seasonal Energy Transfer Mechanism (SETM) (Hu et al., 2022), which we find to be active in both model generations. The physical chain is as follows (Fig. 11): Enhanced summer insolation during the MH drives substantial sea ice melt, leading to a significant expansion of open water relative to the PI in JJA (Figs. 11a, 11d). The replacement of high-albedo, low-heat-capacity ice by low-albedo, high-heat-capacity open water allows greater absorption and subsurface storage of solar radiation (Sejas et al., 2014; Shi and Lohmann, 2024). This storage manifests as the summer

https://doi.org/10.5194/egusphere-2026-664
Preprint. Discussion started: 5 February 2026

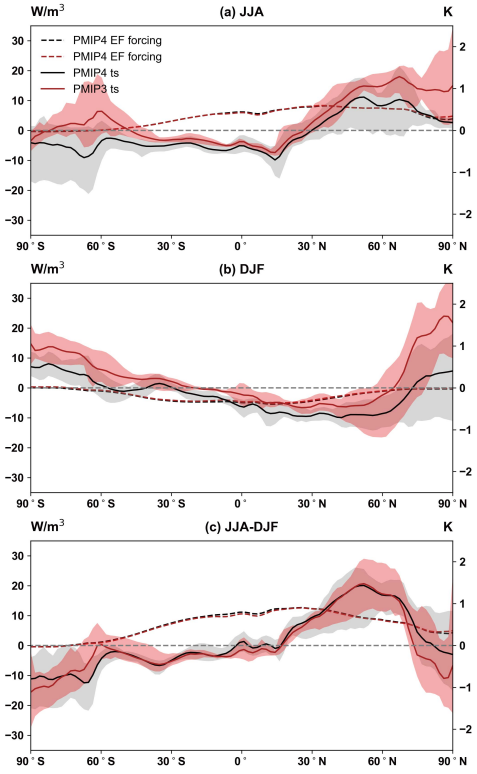

Figure 9. Zonal variations of mean radiation and mean temperature changes (MH-PI). (a) and (b) Distributions for JJA and DJF, respectively, and (c) shows their difference.The solid lines denote the MME mean, and the shaded areas indicate the spread across individual models.

cooling effect in the CFRAM SRF/OCH term (Figs. 10c, 10g). In DJF, despite little change in sea ice extent compared to PI (Figs. 11c, 11e), heat accumulated in the upper ocean during summer is released back to the atmosphere through enhanced turbulent fluxes and delayed autumn freeze-up, generating anomalous winter warming (Yang et al., 2015). This mechanism, analogous to the observed modern ocean-ice-atmosphere coupling mechanism (Zhang et al., 2023), effectively transduces intense summer insolation into a delayed winter warming signal (Figs. 11c, 11g), producing a seasonal temperature anomaly structure opposite to expected seasonal temperature response dictated by orbital forcing alone.

4.3 Mechanisms underlying seasonal temperature differences

While the SETM operates in both generations, its strength—and therefore the amplitude of the seasonal temperature anomalies—differs markedly due to the background climate state set by GHG. In PMIP3, under a warmer background, precessional forcing triggers strong summer sea ice retreat (Fig. 11a), resulting in a large seasonal ice range (Fig. 11c) and vigorous oceanic heat uptake. This fuels a powerful SETM, leading to pronounced winter heat release and strong annual-mean warming. In PMIP4, lower GHG concentrations create a cooler mean state, which buffers the cryospheric response. Summer sea ice melt

https://doi.org/10.5194/egusphere-2026-664
Preprint. Discussion started: 5 February 2026

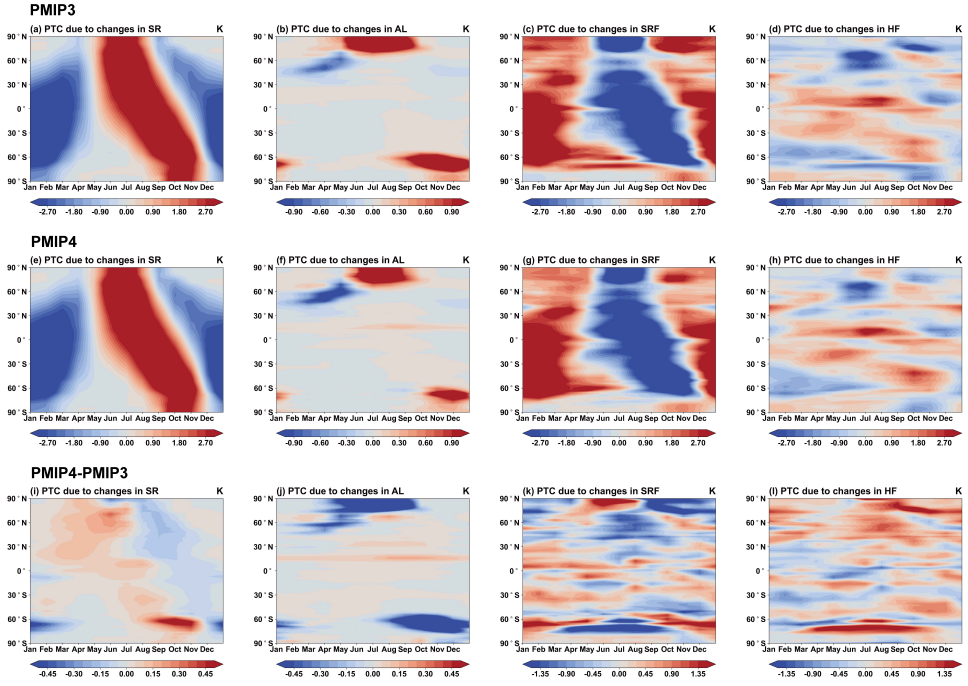

Figure 10. Contributions of individual feedback processes to seasonal temperature changes in PMIP3 and PMIP4.

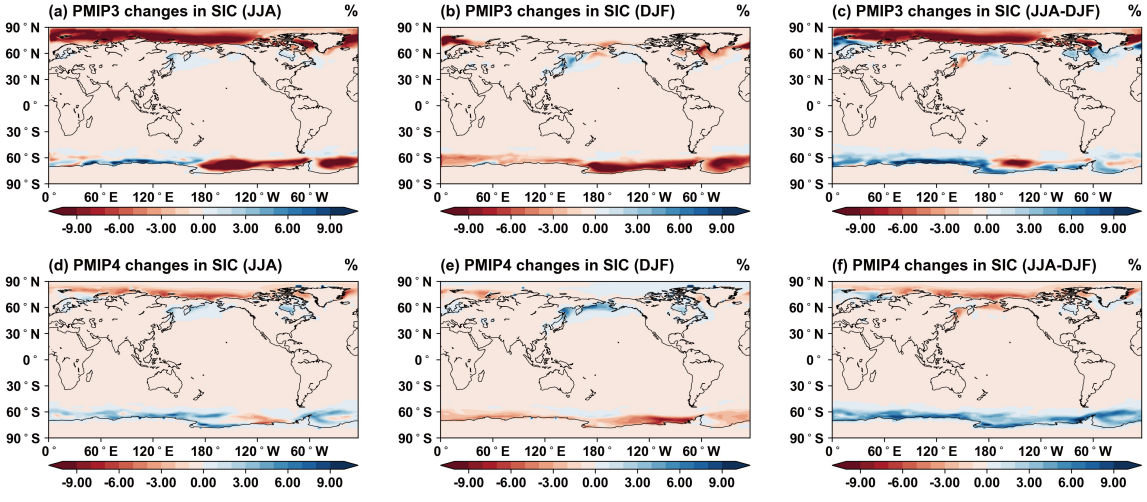

Figure 11. Seasonal changes in SIC (MH-PI).

https://doi.org/10.5194/egusphere-2026-664
Preprint. Discussion started: 5 February 2026

is more limited (Fig. 11d), the seasonal ice cycle is damped (Fig. 11f), and consequently, the ocean's heat storage capacity is reduced. This weakens the entire SETM, resulting in less summer heat uptake and a diminished winter warming effect (Fig. 11g).

These results highlight a nonlinear interaction between orbital forcing and greenhouse gas levels in regulating Arctic climate sensitivity. The Arctic Ocean, a semi-enclosed basin with strong ice-albedo feedback and limited heat capacity, is exquisitely sensitive to summer insolation anomalies (Yin and Berger, 2012). The MH precession provides the energy to drive the SETM, but the efficacy of this mechanism is gated by the background temperature, which controls the initial ice cover and melt potential. The cooler PMIP4 climate therefore nonlinearly suppresses the Arctic temperature response by limiting the first step in the SETM chain—summer ice melt and subsequent ocean heat absorption. This interaction elegantly explains why the difference in Arctic warming between PMIP3 and PMIP4 is so pronounced, extending beyond the annual mean to fundamentally alter the character of the seasonal cycle itself.

5 Consistency assessment between the model and records

The substantial climatic differences between the two model generations underscore the need to evaluate their performance against proxy-based reconstructions, particularly in the mid-to-high latitude Northern Hemisphere. To further assess their simulation performance, we compare the simulated MH temperatures from PMIP3 and PMIP4 with two independent reconstructions: the pollen-based reconstructions and machine-learning-based brGDGT-DLNN reconstructions.

For the annual mean temperature, pollen-based reconstructions suggest widespread warming trend across the Northern Hemisphere, strongest at high latitudes (∼0.6 K), albeit with considerable spread (Fig. 12a). The brGDGT-DLNN reconstructions, in contrast, indicates mid-latitude cooling of approximately 0.9 K at 20°N-50°N. PMIP3 simulates a warm pattern that is broadly consistent with the pollen data, showing mid-to-high latitude warming (up to 0.4 K at 70°N-80°N). PMIP4 simulates overall cooler conditions, showing better spatial correspondence with the brGDGT-DLNN cooling signal. Regarding summer (JJA) temperatures (Fig. 12b), all datasets agree on Northern Hemisphere warming during the MH. PMIP3 showing the greatest warming magnitude, whereas PMIP4 exhibits closer agreement with both the pollen and brGDGT-DLNN reconstructions. The most striking discrepancy emerges in winter (DJF) (Fig. 12c). In the low latitudes, especially at 20°N-30°N, pollen reconstructions generally show warming even exceeding 1 K, while both model generations simulate cooling, with a larger magnitude in PMIP4.

Apparently, the model-proxy discrepancy is most acute in winter, pointing to a fundamental inconsistency. Two potential sources of this issue exist: a model deficiency in transferring summer heat to winter, or a proxy bias toward growing-season conditions. A common model bias is seasonal energy transfer, leading to overly cold winter simulations (Zhang et al., 2022). However, our CFRAM results show that both PMIP3 and PMIP4 exhibit a strong Seasonal Energy Transfer Mechanism (SETM), where summer oceanic heat uptake (SRF as a sink) is efficiently released in winter (SRF as a source) (Figs. 10c, 10g). This demonstrates that the models are physically capable of generating winter warming from summer insolation. A well-documented bias in vegetation-based (e.g., pollen) proxies is their inherent sensitivity to growing-season (primarily summer) temperatures,

https://doi.org/10.5194/egusphere-2026-664
Preprint. Discussion started: 5 February 2026

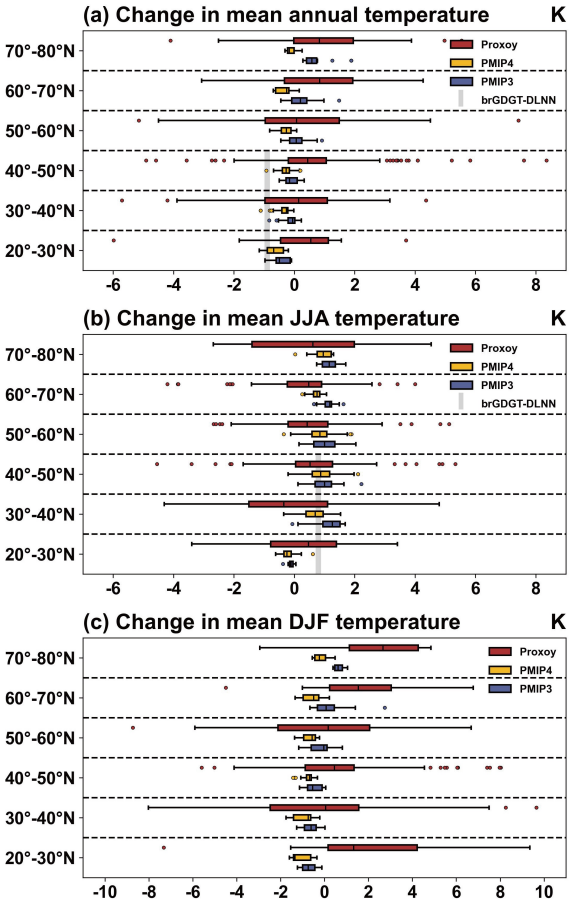

Figure 12. Zonal mean temperatures in the Northern Hemisphere reconstructed from proxy records, brGDGT-DLNN, PMIP3, and PMIP4.

with limited or biased sensitivity to winter conditions (Chen et al., 2023a; Liu et al., 2025). This likely leads to an overestimation of temperature changes annual, and particularly winter, warmth when seasonal signals are not deconvolved. The cooler annual mean signal reconstructed by brGDGT-DLNN, which more completely integrates annual signals, further supports the interpretation that pollen-based reconstructions overestimate the MH warming, especially in winter.

Moreover, the agreement between PMIP3 and pollen-based reconstructions in annual mean temperatures can be understood as an error compensation: the overly MH warming in PMIP3 due to lower GHG concentrations coincidentally matches the pollen-based overestimation due to the missing winter cooling signal. By contrast, PMIP4 shows better agreement with both pollen and brGDGT-DLNN in summer. Meanwhile, the annual mean reconstruction from brGDGT-DLNN further supports a cooler MH climate. When the potential winter overestimation in proxy records is taken into account, PMIP4—although slightly cooler overall—shows better consistency with multiple independent proxies in both annual mean and summer temper-

https://doi.org/10.5194/egusphere-2026-664
Preprint. Discussion started: 5 February 2026

atures. Therefore, PMIP4 is likely more reliable in representing the MH climate, which can be attributed to its more accurate greenhouse gas parameter settings.

6 Conclusions

This study systematically analyzes the temperature differences between PMIP3 and PMIP4 simulations of the MH climate. Using the CFRAM method, we quantitatively assess the contributions of different feedback processes to the annual and seasonal climate responses. Results show that the PMIP3-PMIP4 discrepancy is determined by the changes in EF, which includes the spatiotemporal redistribution of radiation associated with orbital parameters and the overall cooling effect of reduced GHG concentrations. As the EF changes, a series of feedbacks—notably AL and SRF—amplify temperature anomalies with increasing latitude, leading to more pronounced polar warming, a feature consistent with modern climate processes. In PMIP4, the lower GHG concentrations partially offset the warming effect of enhanced SR at mid- to high latitudes, resulting in cooling patterns that distinguish it from PMIP3 in these regions.

Changes in Earth's orbital parameters make a substantial contribution to polar warming during the MH. In Antarctica, increased obliquity enhances solar absorption over the surrounding open ocean and weakens the ACC, thereby amplifying Antarctic warming. In the Arctic, precession-driven changes in seasonal insolation strengthen seasonal contrast: summer sea-ice retreat and expanded open water promote greater ocean heat uptake and storage, and the stored heat is subsequently released to the atmosphere in winter, intensifying Arctic warmingb(Fig. 13).

On the other hand, GHG effects suppress the magnitude of polar amplification. In PMIP3, GHG concentrations remain similar to PI levels, allowing the full expression of the polar amplification effect induced by SR. In PMIP4, however, substantially lower GHG concentrations offset the warming associated with increased shortwave radiation at both poles. Thus, reduced GHG levels not only exert a direct cooling influence on global temperatures but also diminish the nonlinear polar amplification, constituting a key source of the differences between the two model generations (Fig. 13).

Through a multi-proxy and model comparison, we find that traditional pollen-based reconstructions show substantial wintertime deviations from the model simulations, likely due to their strong sensitivity to growing-season conditions. Overall, PMIP4 shows better agreement with independent proxies (e.g., the brGDGT-DLNN reconstruction) in terms of both the spatial distribution and magnitude of annual mean and summer temperatures, which may be related to its use of GHG settings closer to the actual MH conditions. Given that PMIP4 also exhibits a cooler simulated climate, we therefore tend to support a relatively cooler MH. Nonetheless, significant discrepancies remain between models and data, underscoring the need for further improvement in future research.

Our study highlights the joint regulatory effects of orbital parameters and GHG changes on MH temperatures. The temperature differences between the two model generations are not merely the direct consequence of reduced GHG concentrations, but also reflect the nonlinear temperature responses arising from the interaction between these two external forcings. Under future conditions of increasing GHG levels, a decrease in Earth's obliquity and a reduction in precession may partially weaken polar amplification. Our findings reveal the coupled roles of GHG forcing and orbital forcing in MH polar warming mechanisms

https://doi.org/10.5194/egusphere-2026-664
Preprint. Discussion started: 5 February 2026

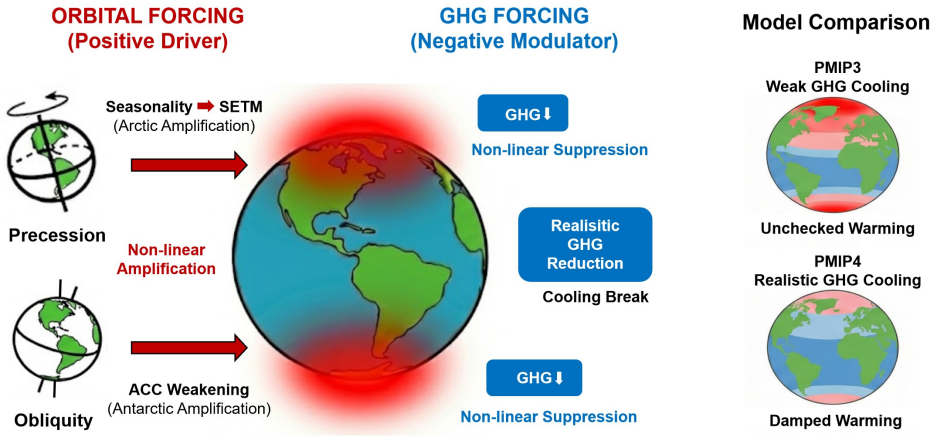

Figure 13. Coupled roles of orbital forcing and GHG forcing in modulating polar warming during the Mid-Holocene.

and emphasize the importance of climate feedback processes and seasonal energy exchange in amplifying regional differences, thereby providing physical constraints for predicting polar temperature responses in future scenarios.

Data availability. The required output variables from the PMIP3 and PMIP4 midHolocene and piControl simulations are freely available from the Earth System Grid Federation (ESGF) at https://aims2.llnl.gov/search (last access: 10 December 2025). Details of the specific model outputs used in this study are provided in Table 2. Pollen-based temperature reconstructions are obtained from the Temperature 12k database (https://lipdverse.org/project/temp12k/), which provides latitudinal-band and global temperature reconstructions derived using multiple statistical approaches. Additional seasonal temperature reconstructions for the Northern Hemisphere landmass are taken from Zhang et al. (2022), whose supplementary data are available at https://www.nature.com/articles/s41467-022-33107-0. The brGDGT-DLNN machine-learning temperature reconstructions of Liu et al. (2025) are available directly from the original publication.

https://doi.org/10.5194/egusphere-2026-664
Preprint. Discussion started: 5 February 2026

Appendix A

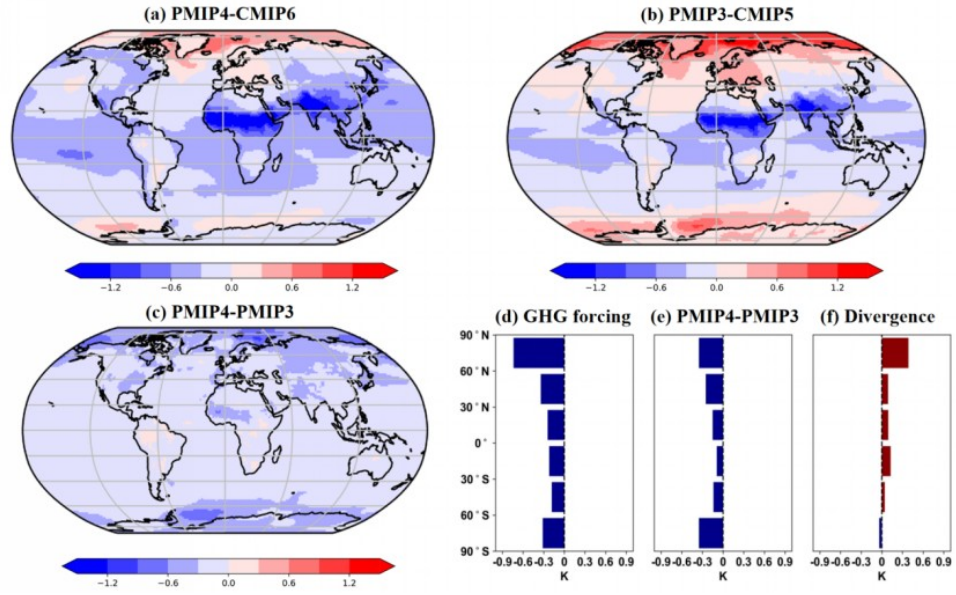

Figure A1. Differences in MH temperature changes between PMIP3 and PMIP4. (a) MH temperature changes simulated by PMIP4. (b) MH temperature changes simulated by PMIP3. (c) Temperature differences between PMIP4 and PMIP3 simulations. (d) Contribution of GHG to the zonal temperature differences between the two model generations, as estimated by Brierley et al. (2020). (e) Zonal temperature differences between PMIP4 and PMIP3. (f) The temperature discrepancies between the two model generations that cannot be explained by GHG forcings, i.e. the difference between (e) and (d).

https://doi.org/10.5194/egusphere-2026-664
Preprint. Discussion started: 5 February 2026

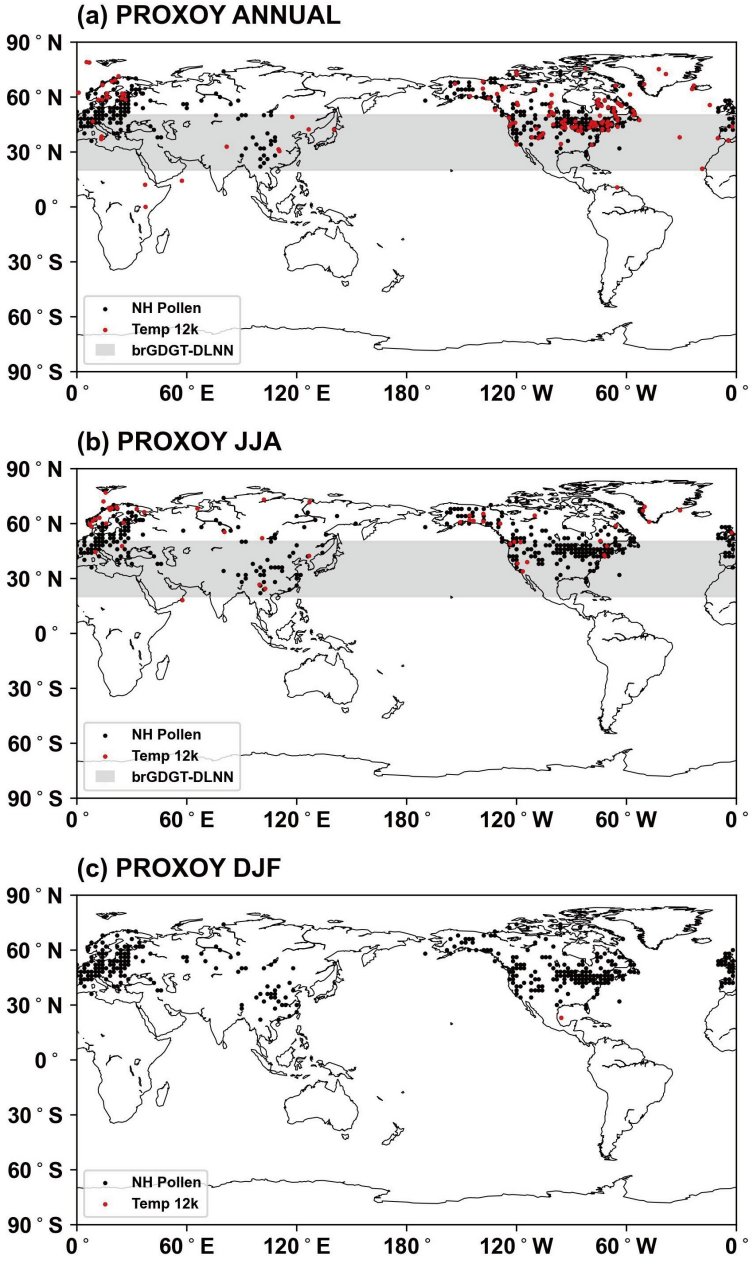

Figure A2. Locations of proxy records. (a), (b) and (c) The spatial coverage of the proxy datasets for annual mean, summer (JJA), and winter (DJF), respectively. The brGDGT-DLNN dataset (shaded gray band) is shown as the mean over 20°N-50°N.

https://doi.org/10.5194/egusphere-2026-664
Preprint. Discussion started: 5 February 2026

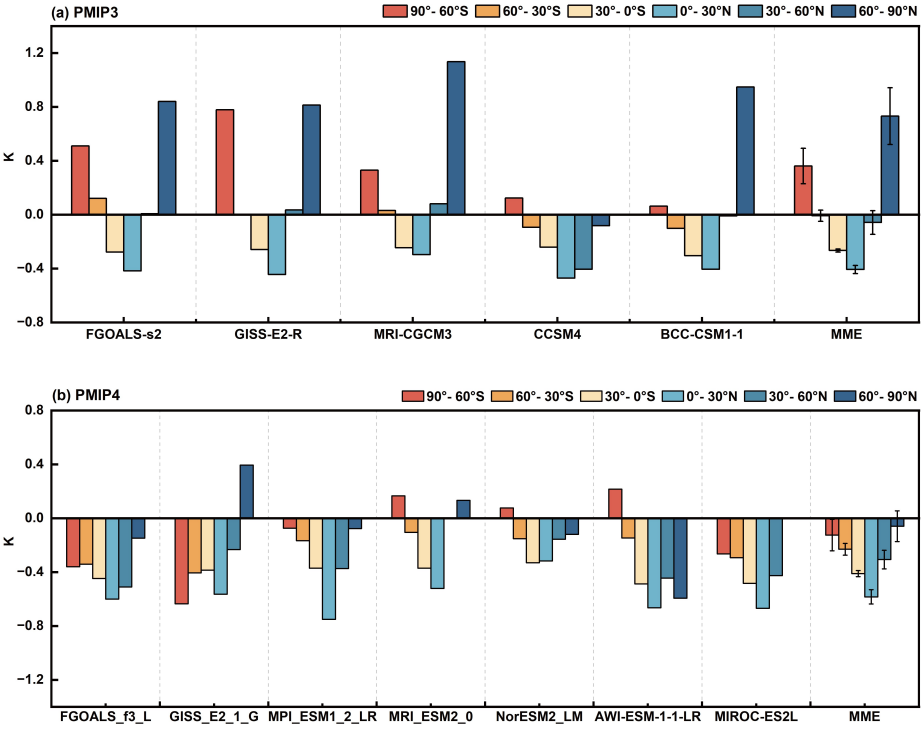

Figure A3. Zonal mean MH temperature changes and differences for individual models and the MME of PMIP3 and PMIP4.

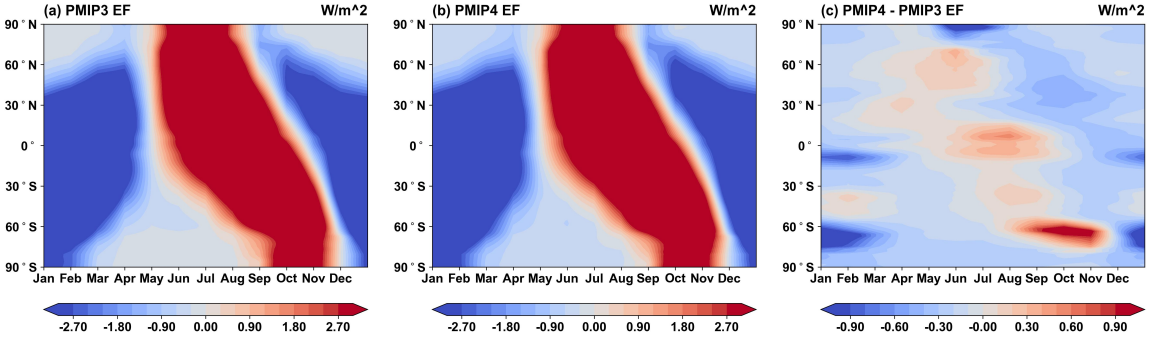

Figure A4. External forcing changes (MH-PI) and differences in the two generations of models. (a) and (b) Changes simulated by the PMIP3 MME and PMIP4 MME, respectively. (c) The difference between PMIP4 and PMIP3.

https://doi.org/10.5194/egusphere-2026-664
Preprint. Discussion started: 5 February 2026

Table A1. GHG specifications in different PMIP3 and PMIP4 models (unit: ppm).

	Model acronym	PI			MH		
		CO_2	N_2O	CH_4	CO_2	N_2O	CH_4
PMIP3–CMIP5	BCC-CSM1-1	284.7	0.276	0.792	280	0.27	0.65
	CCSM4	284.7	0.276	0.792	280	0.27	0.65
	FGOALS-s2	284.0	0.275	0.79	280	0.27	0.65
	GISS-E2-R	285.0	0.275	0.791	280	0.27	0.65
	MRI-CGCM3	284.7	0.275	0.791	280	0.27	0.65
PMIP4–CMIP6	AWI-ESM-1-1-LR	284.3	0.273	0.808	264.4	0.262	0.597
	FGOALS-f3-L	284.3	0.273	0.810	264.4	0.262	0.597
	GISS-E2-1-G	284.3	0.273	0.808	264.4	0.262	0.597
	MIROC-ES2L	284.725	0.273	0.808	264.4	0.262	0.597
	MPI-ESM1-2-LR	284.3	0.273	0.808	264.4	0.262	0.597
	MRI-ESM2-0	284.3	0.273	0.808	264.4	0.262	0.597
	NorESM2-LM	284.3	0.273	0.808	264.4	0.262	0.597

Author contributions. Wenyuan Wang and Hanjie Fan conceptualized the study. Wenyuan Wang performed the CFRAM calculations, analyzed the PMIP3 and PMIP4 model outputs, and prepared the original draft. Xiaoming Hu and Kaiqiang Deng contributed to validation and provided critical feedback on the analyses and figures. Song Yang and Hanjie Fan supervised the project and acquired funding. All authors contributed to interpretation of the results and participated in writing, reviewing, and editing the final manuscript.

Competing interests. The authors declare that they have no conflict of interest.

Acknowledgements. This study is supported by the National Key Research and Development Project of China (2024YFF0506600), the National Natural Science Foundation of China (42575025), the Innovation Group Project of Southern Marine Science and Engineering Guangdong Laboratory (Zhuhai) (316323005) and the Guangdong Province Key Laboratory for Climate Change and Natural Disaster Studies (2023B1212060019).

https://doi.org/10.5194/egusphere-2026-664
Preprint. Discussion started: 5 February 2026

References

Bartlein, P. J., Harrison, S. P., Brewer, S., Connor, S., Davis, B. A. S., Gajewski, K., Guiot, J., Harrison-Prentice, T. I., Henderson, A., Peyron, O., Prentice, I. C., Scholze, M., Seppä, H., Shuman, B., Sugita, S., Thompson, R. S., Viau, A. E., Williams, J., and Wu, H.: Pollen-Based Continental Climate Reconstructions at 6 and 21 Ka: A Global Synthesis, Climate Dynamics, 37, 775–802, https://doi.org/10.1007/s00382-010-0904-1, 2011.

Berger, A.: Long-term variations of caloric insolation resulting from the Earth's orbital elements, Quaternary research, 9, 139–167, 1978.

Bova, S., Rosenthal, Y., Liu, Z., Godad, S. P., and Yan, M.: Seasonal Origin of the Thermal Maxima at the Holocene and the Last Interglacial, Nature, 589, 548–553, https://doi.org/10.1038/s41586-020-03155-x, 2021.

Braconnot, P., Otto-Bliesner, B., Harrison, S., Joussaume, S., Peterchmitt, J.-Y., Abe-Ouchi, A., Crucifix, M., Driesschaert, E., Fichefet, T., Hewitt, C. D., Kageyama, M., Kitoh, A., Laîné, A., Loutre, M.-F., Marti, O., Merkel, U., Ramstein, G., Valdes, P., Weber, S. L., Yu, Y., and Zhao, Y.: Results of PMIP2 Coupled Simulations of the Mid-Holocene and Last Glacial Maximum – Part 1: Experiments and Large-Scale Features, Climate of the Past, 3, 261–277, https://doi.org/10.5194/cp-3-261-2007, 2007.

Brierley, C. M., Zhao, A., Harrison, S. P., Braconnot, P., Williams, C. J. R., Thornalley, D. J. R., Shi, X., Peterschmitt, J.-Y., Ohgaito, R., Kaufman, D. S., Kageyama, M., Hargreaves, J. C., Erb, M. P., Emile-Geay, J., D'Agostino, R., Chandan, D., Carré, M., Bartlein, P. J., Zheng, W., Zhang, Z., Zhang, Q., Yang, H., Volodin, E. M., Tomas, R. A., Routson, C., Peltier, W. R., Otto-Bliesner, B., Morozova, P. A., McKay, N. P., Lohmann, G., Legrande, A. N., Guo, C., Cao, J., Brady, E., Annan, J. D., and Abe-Ouchi, A.: Large-Scale Features and Evaluation of the PMIP4-CMIP6 *midHolocene* Simulations, Climate of the Past, 16, 1847–1872, https://doi.org/10.5194/cp-16-1847-2020, 2020.

Bruno, M. and Joos, F.: Terrestrial Carbon Storage during the Past 200 Years: A Monte Carlo Analysis of CO2 Data from Ice Core and Atmospheric Measurements, Global Biogeochemical Cycles, 11, 111–124, https://doi.org/10.1029/96GB03611, 1997.

Burls, N. and Sagoo, N.: Increasingly Sophisticated Climate Models Need the Out-Of-Sample Tests Paleoclimates Provide, Journal of Advances in Modeling Earth Systems, 14, e2022MS003 389, https://doi.org/10.1029/2022MS003389, 2022.

Cai, M. and Lu, J.: A New Framework for Isolating Individual Feedback Processes in Coupled General Circulation Climate Models. Part II: Method Demonstrations and Comparisons, Climate Dynamics, 32, 887–900, https://doi.org/10.1007/s00382-008-0424-4, 2009.

Chen, F., Duan, Y., Hao, S., Chen, J., Feng, X., Hou, J., Cao, X., Zhang, X., and Zhou, T.: Holocene Thermal Maximum Mode versus the Continuous Warming Mode: Problems of Data-Model Comparisons and Future Research Prospects, Science China Earth Sciences, 66, 1683–1701, https://doi.org/10.1007/s11430-022-1113-x, 2023a.

Chen, J., Zhang, Q., Lu, Z., Duan, Y., Cao, X., Huang, J., and Chen, F.: Reconciling East Asia's Mid-Holocene Temperature Discrepancy through Vegetation-Climate Feedback, Science Bulletin, 69, 2420–2429, https://doi.org/10.1016/j.scib.2024.04.012, 2024.

Chen, W., Zhang, Z., Ciais, P., Tan, L., Kemp, D. B., and Viovy, N.: Enhanced Mid-Holocene Vegetation Growth and Its Biophysical Feedbacks in China, Geophysical Research Letters, 50, e2023GL104 702, https://doi.org/10.1029/2023GL104702, 2023b.

Dufresne, J.-L., Foujols, M.-A., Denvil, S., Caubel, A., Marti, O., Aumont, O., Balkanski, Y., Bekki, S., Bellenger, H., Benshila, R., Bony, S., Bopp, L., Braconnot, P., Brockmann, P., Cadule, P., Cheruy, F., Codron, F., Cozic, A., Cugnet, D., De Noblet, N., Duvel, J.-P., Ethé, C., Fairhead, L., Fichefet, T., Flavoni, S., Friedlingstein, P., Grandpeix, J.-Y., Guez, L., Guilyardi, E., Hauglustaine, D., Hourdin, F., Idelkadi, A., Ghattas, J., Joussaume, S., Kageyama, M., Krinner, G., Labetoulle, S., Lahellec, A., Lefebvre, M.-P., Lefevre, F., Levy, C., Li, Z. X., Lloyd, J., Lott, F., Madec, G., Mancip, M., Marchand, M., Masson, S., Meurdesoif, Y., Mignot, J., Musat, I., Parouty, S., Polcher, J., Rio, C., Schulz, M., Swingedouw, D., Szopa, S., Talandier, C., Terray, P., Viovy, N., and Vuichard, N.: Climate Change Projections Using the

https://doi.org/10.5194/egusphere-2026-664
Preprint. Discussion started: 5 February 2026

IPSL-CM5 Earth System Model: From CMIP3 to CMIP5, Climate Dynamics, 40, 2123–2165, https://doi.org/10.1007/s00382-012-1636-1, 2013.

Emori, S., Taylor, K., Hewitson, B., Zermoglio, F., Juckes, M., Lautenschlager, M., and Stockhause, M.: CMIP5 data provided at the IPCC Data Distribution Centre, Fact Sheet of the task group on data and scenario support for impact and climate analysis (TGICA) of the intergovernmental panel on climate change (IPCC), 8, 2016.

Eyring, V., Bony, S., Meehl, G. A., Senior, C. A., Stevens, B., Stouffer, R. J., and Taylor, K. E.: Overview of the Coupled Model Intercomparison Project Phase 6 (CMIP6) Experimental Design and Organization, Geoscientific Model Development, 9, 1937–1958, https://doi.org/10.5194/gmd-9-1937-2016, 2016.

Fan, H., Hu, X., Yang, S., Choi, Y.-S., and Lee, Y.-K.: Process-Based Analysis of Relative Contributions to the Multi-Model Warming Projection over East Asia, Climate Dynamics, 56, 2729–2747, https://doi.org/10.1007/s00382-020-05614-7, 2021.

Friedrich, T., Timmermann, A., Tigchelaar, M., Elison Timm, O., and Ganopolski, A.: Nonlinear Climate Sensitivity and Its Implications for Future Greenhouse Warming, Science Advances, 2, e1501 923, https://doi.org/10.1126/sciadv.1501923, 2016.

Fu, Q., Liou, K. N., Cribb, M. C., Charlock, T. P., and Grossman, A.: Multiple Scattering Parameterization in Thermal Infrared Radiative Transfer, Journal of the Atmospheric Sciences, 54, 2799–2812, https://doi.org/10.1175/1520-0469(1997)054<2799:MSPITI>2.0.CO;2, 1997.

Giglio, D. and Johnson, G. C.: Subantarctic and Polar Fronts of the Antarctic Circumpolar Current and Southern Ocean Heat and Freshwater Content Variability: A View from Argo, Journal of Physical Oceanography, 46, 749–768, https://doi.org/10.1175/JPO-D-15-0131.1, 2016.

Hargreaves, J. C., Annan, J. D., Ohgaito, R., Paul, A., and Abe-Ouchi, A.: Skill and Reliability of Climate Model Ensembles at the Last Glacial Maximum and Mid-Holocene, Climate of the Past, 9, 811–823, https://doi.org/10.5194/cp-9-811-2013, 2013.

Harrison, S. P., Bartlein, P. J., Brewer, S., Prentice, I. C., Boyd, M., Hessler, I., Holmgren, K., Izumi, K., and Willis, K.: Climate Model Benchmarking with Glacial and Mid-Holocene Climates, Climate Dynamics, 43, 671–688, https://doi.org/10.1007/s00382-013-1922-6, 2014.

Harrison, S. P., Bartlein, P. J., Izumi, K., Li, G., Annan, J., Hargreaves, J., Braconnot, P., and Kageyama, M.: Evaluation of CMIP5 Palaeo-Simulations to Improve Climate Projections, Nature Climate Change, 5, 735–743, https://doi.org/10.1038/nclimate2649, 2015.

Hu, X., Li, Y., Yang, S., Deng, Y., and Cai, M.: Process-Based Decomposition of the Decadal Climate Difference between 2002–13 and 1984–95, Journal of Climate, 30, 4373–4393, https://doi.org/10.1175/JCLI-D-15-0742.1, 2017.

Hu, X., Fan, H., Cai, M., Sejas, S. A., Taylor, P., and Yang, S.: A Less Cloudy Picture of the Inter-Model Spread in Future Global Warming Projections, Nature Communications, 11, 4472, https://doi.org/10.1038/s41467-020-18227-9, 2020.

Hu, X., Liu, Y., Kong, Y., and Yang, Q.: A Quantitative Analysis of the Source of Inter-Model Spread in Arctic Surface Warming Response to Increased CO2 Concentration, Geophysical Research Letters, 49, e2022GL100 034, https://doi.org/10.1029/2022GL100034, 2022.

Jiang, D., Lang, X., Tian, Z., and Wang, T.: Considerable Model–Data Mismatch in Temperature over China during the Mid-Holocene: Results of PMIP Simulations, Journal of Climate, 25, 4135–4153, https://doi.org/10.1175/jcli-d-11-00231.1, 2012.

Jiang, D., Tian, Z., and Lang, X.: Mid-Holocene Global Monsoon Area and Precipitation from PMIP Simulations, Climate Dynamics, 44, 2493–2512, https://doi.org/10.1007/s00382-014-2175-8, 2015.

Kageyama, M., Braconnot, P., Harrison, S. P., Haywood, A. M., Jungclaus, J. H., Otto-Bliesner, B. L., Peterschmitt, J.-Y., Abe-Ouchi, A., Albani, S., Bartlein, P. J., Brierley, C., Crucifix, M., Dolan, A., Fernandez-Donado, L., Fischer, H., Hopcroft, P. O., Ivanovic, R. F., Lambert, F., Lunt, D. J., Mahowald, N. M., Peltier, W. R., Phipps, S. J., Roche, D. M., Schmidt, G. A., Tarasov, L., Valdes, P. J., Zhang, Q.,

https://doi.org/10.5194/egusphere-2026-664
Preprint. Discussion started: 5 February 2026

and Zhou, T.: The PMIP4 Contribution to CMIP6 – Part 1: Overview and over-Arching Analysis Plan, Geoscientific Model Development, 11, 1033–1057, https://doi.org/10.5194/gmd-11-1033-2018, 2018.

Kang, Y. and Yang, H.: Quantifying Effects of Earth Orbital Parameters and Greenhouse Gases on Mid-Holocene Climate, Climate of the Past, 19, 2013–2026, https://doi.org/10.5194/cp-19-2013-2023, 2023.

Kaufman, D. and Broadman, E.: Revisiting the Holocene Global Temperature Conundrum, Nature, 614, 425–435, https://doi.org/10.1038/s41586-022-05536-w, 2023.

Kaufman, D., McKay, N., Routson, C., Erb, M., Dätwyler, C., Sommer, P. S., Heiri, O., and Davis, B.: Holocene Global Mean Surface Temperature, a Multi-Method Reconstruction Approach, Scientific Data, 7, 201, https://doi.org/10.1038/s41597-020-0530-7, 2020.

Kelley, M., Schmidt, G. A., Nazarenko, L. S., Bauer, S. E., Ruedy, R., Russell, G. L., Ackerman, A. S., Aleinov, I., Bauer, M., Bleck, R., Canuto, V., Cesana, G., Cheng, Y., Clune, T. L., Cook, B. I., Cruz, C. A., Del Genio, A. D., Elsaesser, G. S., Faluvegi, G., Kiang, N. Y., Kim, D., Lacis, A. A., Leboissetier, A., LeGrande, A. N., Lo, K. K., Marshall, J., Matthews, E. E., McDermid, S., Mezuman, K., Miller, R. L., Murray, L. T., Oinas, V., Orbe, C., García-Pando, C. P., Perlwitz, J. P., Puma, M. J., Rind, D., Romanou, A., Shindell, D. T., Sun, S., Tausnev, N., Tsigaridis, K., Tselioudis, G., Weng, E., Wu, J., and Yao, M.-S.: GISS-E2.1: Configurations and Climatology, Journal of Advances in Modeling Earth Systems, 12, e2019MS002 025, https://doi.org/10.1029/2019MS002025, 2020.

Lamy, F., Chiang, J. C. H., Martínez-Méndez, G., Thierens, M., Arz, H. W., Bosmans, J., Hebbeln, D., Lambert, F., Lembke-Jene, L., and Stuut, J.-B.: Precession Modulation of the South Pacific Westerly Wind Belt over the Past Million Years, Proceedings of the National Academy of Sciences, 116, 23 455–23 460, https://doi.org/10.1073/pnas.1905847116, 2019.

Li, L., Lin, P., Yu, Y.-Q., Wang, B., Zhou, T., Liu, l., Liu, H., Bao, Q., Xu, S., and Huang, W.: The Flexible Global Ocean-Atmosphere-Land System Model, Grid-point Version 2: FGOALS-g2, Advances in Atmospheric Sciences, 30, 543–560, 2013.

Lin, Y., Ramstein, G., Wu, H., Rani, R., Braconnot, P., Kageyama, M., Li, Q., Luo, Y., Zhang, R., and Guo, Z.: Mid-Holocene Climate Change over China: Model–Data Discrepancy, Climate of the Past, 15, 1223–1249, https://doi.org/10.5194/cp-15-1223-2019, 2019.

Liu, Z., Zhu, J., Rosenthal, Y., Zhang, X., Otto-Bliesner, B. L., Timmermann, A., Smith, R. S., Lohmann, G., Zheng, W., and Elison Timm, O.: The Holocene Temperature Conundrum, Proceedings of the National Academy of Sciences, 111, https://doi.org/10.1073/pnas.1407229111, 2014.

Liu, Z., Cheng, J., Zheng, Y., Zhang, W., Liu, H., Wu, H., Zhu, J., and Xie, S.: The Seasonal Temperature Conundrum for the Holocene, Science AdvAnceS, 2025.

Mauritsen, T., Bader, J., Becker, T., Behrens, J., Bittner, M., Brokopf, R., Brovkin, V., Claussen, M., Crueger, T., Esch, M., Fast, I., Fiedler, S., Fläschner, D., Gayler, V., Giorgetta, M., Goll, D. S., Haak, H., Hagemann, S., Hedemann, C., Hohenegger, C., Ilyina, T., Jahns, T., Jimenéz-de-la Cuesta, D., Jungclaus, J., Kleinen, T., Kloster, S., Kracher, D., Kinne, S., Kleberg, D., Lasslop, G., Kornblueh, L., Marotzke, J., Matei, D., Meraner, K., Mikolajewicz, U., Modali, K., Möbis, B., Müller, W. A., Nabel, J. E. M. S., Nam, C. C. W., Notz, D., Nyawira, S.-S., Paulsen, H., Peters, K., Pincus, R., Pohlmann, H., Pongratz, J., Popp, M., Raddatz, T. J., Rast, S., Redler, R., Reick, C. H., Rohrschneider, T., Schemann, V., Schmidt, H., Schnur, R., Schulzweida, U., Six, K. D., Stein, L., Stemmler, I., Stevens, B., Von Storch, J.-S., Tian, F., Voigt, A., Vrese, P., Wieners, K.-H., Wilkenskjeld, S., Winkler, A., and Roeckner, E.: Developments in the MPI-M Earth System Model Version 1.2 (MPI-ESM1.2) and Its Response to Increasing CO_2, Journal of Advances in Modeling Earth Systems, 11, 998–1038, https://doi.org/10.1029/2018MS001400, 2019.

Ohgaito, R., Yamamoto, A., Hajima, T., O'ishi, R., Abe, M., Tatebe, H., Abe-Ouchi, A., and Kawamiya, M.: PMIP4 Experiments Using MIROC-ES2L Earth System Model, Geoscientific Model Development, 14, 1195–1217, https://doi.org/10.5194/gmd-14-1195-2021, 2021.

https://doi.org/10.5194/egusphere-2026-664
Preprint. Discussion started: 5 February 2026

Otto-Bliesner, B. L., Braconnot, P., Harrison, S. P., Lunt, D. J., Abe-Ouchi, A., Albani, S., Bartlein, P. J., Capron, E., Carlson, A. E., Dutton, A., Fischer, H., Goelzer, H., Govin, A., Haywood, A., Joos, F., LeGrande, A. N., Lipscomb, W. H., Lohmann, G., Mahowald, N., Nehrbass-Ahles, C., Pausata, F. S. R., Peterschmitt, J.-Y., Phipps, S. J., Renssen, H., and Zhang, Q.: The PMIP4 Contribution to CMIP6 – Part 2: Two Interglacials, Scientific Objective and Experimental Design for Holocene and Last Interglacial Simulations, Geoscientific Model Development, 10, 3979–4003, https://doi.org/10.5194/gmd-10-3979-2017, 2017.

Park, H.-S., Kim, S.-J., Seo, K.-H., Stewart, A. L., Kim, S.-Y., and Son, S.-W.: The Impact of Arctic Sea Ice Loss on Mid-Holocene Climate, Nature Communications, 9, 4571, https://doi.org/10.1038/s41467-018-07068-2, 2018.

Sahany, S., Mishra, S. K., and Salunke, P.: Historical Simulations and Climate Change Projections over India by NCAR CCSM4: CMIP5 vs. NEX-GDDP, Theoretical and Applied Climatology, 135, 1423–1433, https://doi.org/10.1007/s00704-018-2455-z, 2019.

Sejas, S. A., Cai, M., Hu, A., Meehl, G. A., Washington, W., and Taylor, P. C.: Individual Feedback Contributions to the Seasonality of Surface Warming, Journal of Climate, 27, 5653–5669, https://doi.org/10.1175/JCLI-D-13-00658.1, 2014.

Seland, Ø., Bentsen, M., Olivié, D., Toniazzo, T., Gjermundsen, A., Graff, L. S., Debernard, J. B., Gupta, A. K., He, Y.-C., Kirkevåg, A., Schwinger, J., Tjiputra, J., Aas, K. S., Bethke, I., Fan, Y., Griesfeller, J., Grini, A., Guo, C., Ilicak, M., Karset, I. H. H., Landgren, O., Liakka, J., Moseid, K. O., Nummelin, A., Spensberger, C., Tang, H., Zhang, Z., Heinze, C., Iversen, T., and Schulz, M.: Overview of the Norwegian Earth System Model (NorESM2) and Key Climate Response of CMIP6 DECK, Historical, and Scenario Simulations, Geoscientific Model Development, 13, 6165–6200, https://doi.org/10.5194/gmd-13-6165-2020, 2020.

Shi, J. and Lohmann, G.: Considerable Uncertainty of Simulated Arctic Temperature Change in the Mid-Holocene Due To Initial Ocean Perturbation, Geophysical Research Letters, 51, e2023GL106 337, https://doi.org/10.1029/2023GL106337, 2024.

Shi, X., Werner, M., Wang, Q., Yang, H., and Lohmann, G.: Simulated Mid-Holocene and Last Interglacial Climate Using Two Generations of AWI-ESM, Journal of Climate, 35, 7811–7831, https://doi.org/10.1175/JCLI-D-22-0354.1, 2022.

Shi, X., Cauquoin, A., Lohmann, G., Jonkers, L., Wang, Q., Yang, H., Sun, Y., and Werner, M.: Simulated Stable Water Isotopes during the Mid-Holocene and Pre-Industrial Periods Using AWI-ESM-2.1-Wiso, Geoscientific Model Development, 16, 5153–5178, https://doi.org/10.5194/gmd-16-5153-2023, 2023.

Steig, E. J.: Mid-Holocene Climate Change, Science, 286, 1485–1487, https://doi.org/10.1126/science.286.5444.1485, 1999.

Sun, Y., Wu, H., Ramstein, G., Liu, B., Zhao, Y., Li, L., Yuan, X., Zhang, W., Li, L., Zou, L., and Zhou, T.: Revisiting the Physical Mechanisms of East Asian Summer Monsoon Precipitation Changes during the Mid-Holocene: A Data–Model Comparison, Climate Dynamics, 60, 1009–1022, https://doi.org/10.1007/s00382-022-06359-1, 2023.

Taylor, K. E., Stouffer, R. J., and Meehl, G. A.: An Overview of CMIP5 and the Experiment Design, Bulletin of the American Meteorological Society, 93, 485–498, https://doi.org/10.1175/BAMS-D-11-00094.1, 2012.

Ullman, D. J., LeGrande, A. N., Carlson, A. E., Anslow, F. S., and Licciardi, J. M.: Assessing the Impact of Laurentide Ice Sheet Topography on Glacial Climate, Climate of the Past, 10, 487–507, https://doi.org/10.5194/cp-10-487-2014, 2014.

Wanner, H., Mercolli, L., Grosjean, M., and Ritz, S. P.: Holocene Climate Variability and Change; a Data-Based Review, Journal of the Geological Society, 172, 254–263, https://doi.org/10.1144/jgs2013-101, 2015.

Wu, T., Song, L., Li, W., Wang, Z., Zhang, H., Xin, X., Zhang, Y., Zhang, L., Li, J., Wu, F., Liu, Y., Zhang, F., Shi, X., Chu, M., Zhang, J., Fang, Y., Wang, F., Lu, Y., Liu, X., Wei, M., Liu, Q., Zhou, W., Dong, M., Zhao, Q., Ji, J., Li, L., and Zhou, M.: An Overview of BCC Climate System Model Development and Application for Climate Change Studies, Journal of Meteorological Research, 28, 34–56, https://doi.org/10.1007/s13351-014-3041-7, 2014.

https://doi.org/10.5194/egusphere-2026-664
Preprint. Discussion started: 5 February 2026

Yang, H., Zhao, Y., Liu, Z., Li, Q., He, F., and Zhang, Q.: Heat Transport Compensation in Atmosphere and Ocean over the Past 22,000 Years, Scientific Reports, 5, 16 661, https://doi.org/10.1038/srep16661, 2015.

Yin, Q. Z. and Berger, A.: Individual Contribution of Insolation and CO2 to the Interglacial Climates of the Past 800,000 Years, Climate Dynamics, 38, 709–724, https://doi.org/10.1007/s00382-011-1013-5, 2012.

Yukimoto, S., Adachi, Y., Hosaka, M., Sakami, T., Yoshimura, H., Hirabara, M., Tanaka, T. Y., Shindo, E., Tsujino, H., Deushi, M., Mizuta, R., Yabu, S., Obata, A., Nakano, H., Koshiro, T., Ose, T., and Kitoh, A.: A New Global Climate Model of the Meteorological Research Institute: MRI-CGCM3 —Model Description and Basic Performance—, Journal of the Meteorological Society of Japan. Ser. II, 90A, 23–64, https://doi.org/10.2151/jmsj.2012-A02, 2012.

Yukimoto, S., Kawai, H., Koshiro, T., Oshima, N., Yoshida, K., Urakawa, S., Tsujino, H., Deushi, M., Tanaka, T., Hosaka, M., Yabu, S., Yoshimura, H., Shindo, E., Mizuta, R., Obata, A., Adachi, Y., and Ishii, M.: The Meteorological Research Institute Earth System Model Version 2.0, MRI-ESM2.0: Description and Basic Evaluation of the Physical Component, Journal of the Meteorological Society of Japan. Ser. II, 97, 931–965, https://doi.org/10.2151/jmsj.2019-051, 2019.

Zelinka, M. D., Myers, T. A., McCoy, D. T., Po-Chedley, S., Caldwell, P. M., Ceppi, P., Klein, S. A., and Taylor, K. E.: Causes of Higher Climate Sensitivity in CMIP6 Models, Geophysical Research Letters, 47, e2019GL085 782, https://doi.org/10.1029/2019GL085782, 2020.

Zhang, W., Wu, H., Geng, J., and Cheng, J.: Model-Data Divergence in Global Seasonal Temperature Response to Astronomical Insolation during the Holocene, Science Bulletin, 67, https://doi.org/10.1016/j.scib.2021.09.004, 2021.

Zhang, W., Wu, H., Cheng, J., Geng, J., Li, Q., Sun, Y., Yu, Y., Lu, H., and Guo, Z.: Holocene Seasonal Temperature Evolution and Spatial Variability over the Northern Hemisphere Landmass, Nature Communications, 13, 5334, https://doi.org/10.1038/s41467-022-33107-0, 2022.

Zhang, Y., Kong, Y., Yang, S., and Hu, X.: Asymmetric Arctic and Antarctic Warming and Its Intermodel Spread in CMIP6, Journal of Climate, 36, 8299–8310, https://doi.org/10.1175/JCLI-D-23-0118.1, 2023.

Zheng, W., Yu, Y., Luan, Y., Zhao, S., He, B., Dong, L., Song, M., Lin, P., and Liu, H.: CAS-FGOALS Datasets for the Two Interglacial Epochs of the Holocene and the Last Interglacial in PMIP4, Advances in Atmospheric Sciences, 37, 1034–1044, https://doi.org/10.1007/s00376-020-9290-8, 2020.